Computational Identification of Taxus baccata-Derived Phytochemicals Targeting EZH2 to Overcome Therapeutic Resistance in Melanoma

Pritom Kundu
Center for Health, Innovation, Research, Action, and Learning - Bangladesh
Musab Shahariar
Center for Health, Innovation, Research, Action, and Learning - Bangladesh
Farzana Akter Munny
Center for Health, Innovation, Research, Action, and Learning - Bangladesh
Anisha Tashruba Riya
Center for Health, Innovation, Research, Action, and Learning - Bangladesh
Hafeza Bhuiyan Lota
Center for Health, Innovation, Research, Action, and Learning - Bangladesh
Md. Zabir Ahmed
Center for Health, Innovation, Research, Action, and Learning - Bangladesh
Mst.Afsana Meme
Center for Health, Innovation, Research, Action, and Learning - Bangladesh
Umme Mahfuza Parvin Kona
Center for Health, Innovation, Research, Action, and Learning - Bangladesh
Fatema Mahmuda
Center for Health, Innovation, Research, Action, and Learning - Bangladesh
Shaima Saif Chowdhury
Center for Health, Innovation, Research, Action, and Learning - Bangladesh
Sadia Afrin Sraboni
Center for Health, Innovation, Research, Action, and Learning - Bangladesh
Md. Jubayer Hossain
contact.jubayerhossain@gmail.com

Center for Health, Innovation, Research, Action, and Learning - Bangladesh

---

Article

Keywords: Therapy resistant Melanoma, Phytochemicals, Molecular Docking, ADMET, DFT, MD Simulation

Posted Date: January 22nd, 2026

DOI: https://doi.org/10.21203/rs.3.rs-8494315/v1

Additional Declarations: No competing interests reported.

Computational Identification of *Taxus baccata*-Derived Phytochemicals Targeting EZH2 to Overcome Therapeutic Resistance in Melanoma

Pritom Kundu[3,4 †], Musab Shahariar[3,5 †], Farzana Akter Munny[3,6], Anisha Tashruba Riya[3,7], Hafeza Bhuiyan Lota[3,8], Md. Zabir Ahmed[3,8], Mst. Afsana Meme[3,9], Umme Mahfuza Parvin Kona[3,9], Fatema Mahmuda[1,10], Shaima Saif Chowdhury[1,11], Sadia Afrin Sraboni[1,12] Md. Jubayer Hossain[1,2*]

[1]Center for Health Innovation, Research Action, and Learning—Bangladesh (CHIRAL Bangladesh), Dhaka 1205, Bangladesh

[2]Department of Public Health, Daffodil International University, Dhaka 1216, Bangladesh

[3]Big Bioinformatics Lab, Center for Health Innovation, Research, Action, and Learning Bangladesh (CHIRAL Bangladesh), Dhaka, Bangladesh

[4]Department of Pharmacy, Faculty of Science, University of Rajshahi, Rajshahi 6205, Bangladesh

[5]Department of Pharmacy, Faculty of Biological Sciences, Islamic University, Kushtia-7003, Bangladesh

[6]Department of Pharmaceutical Chemistry, Faculty of Pharmacy, University of Dhaka, Dhaka 1000, Bangladesh

[7]Biotechnology and Genetic Engineering Discipline, Khulna University, Sher-E-Bangla Rd, Khulna 9208, Bangladesh

[8]Department of Microbiology, Jagannath University, 9-10, Chittaranjan Ave, Dhaka 1100 Bangladesh

[9]Department of Pharmacy, Jahangirnagar University, Savar, Dhaka-1342, Bangladesh

[10]Department of Applied Chemistry and Chemical engineering, Noakhali Science and Technology University, Sonapur, Noakhali, Bangladesh

[11]Department of Botany, University of Chittagong, University of Chittagong Road, Hathazari, Chattogram 4331, Bangladesh.

[12]Department of Pharmacy, University of Asia Pacific, 74/A, Green Road, Farmgate Dhaka-1205, Bangladesh

† These authors contributed equally in this study

*Corresponding author: Md. Jubayer Hossain, Email: contact.jubayerhossain@gmail.com

Abstract

Therapy resistance remains a significant challenge in melanoma treatment, despite recent advances in targeted therapies and immunotherapies. Enhancer of zeste homolog 2 (EZH2) has been identified as a critical target for overcoming resistance. However, the availability of effective inhibitors remains limited, emphasizing the need for novel therapeutic strategies to address this issue. This study aimed to identify potential EZH2 inhibitors derived from *Taxus baccata* using computational methods to overcome melanoma therapy resistance. A total of 98 phytochemical compounds from *Taxus baccata* were selected for in silico screening. The compounds were assessed using molecular docking to predict their binding affinities with EZH2. The pharmacokinetic properties of the compounds were evaluated using ADMET analysis, and Density Functional Theory (DFT) was used to assess their electronic properties. The top compounds were subjected to 100 ns molecular dynamics (MD) simulations to examine their stability and interaction dynamics, using tazemetostat and GSK-126 as reference inhibitors. Among the screened compounds, sotetsuflavone, ginkgetin, amentoflavone, and podocarpusflavone A were identified as potential EZH2 inhibitors. amentoflavone exhibited the highest binding affinity, strong interaction stability, and favorable pharmacokinetic profile. It also demonstrated the lowest negative binding free energy (MMPBSA), indicating a superior binding strength. These findings suggest that amentoflavone is the most promising candidate for further development, with the other compounds providing valuable scaffolds for optimization. This study provides a computational basis for designing novel EZH2 inhibitors from *Taxus baccata*. Further experimental validation is required to confirm these findings and explore the potential therapeutic applications of these phytochemicals in clinical settings.

Keywords: Therapy resistant Melanoma, Phytochemicals, Molecular Docking, ADMET, DFT, MD Simulation

1. Introduction

Melanoma is the most aggressive form of skin cancer, originating from genetic alterations in melanocytes and characterized by high metastatic potential[1,2]. Its global incidence has risen sharply, with an estimated 104,960 new cases projected in 2025[3,4] and a 1.7% increase in mortality anticipated for the same year[5]. Despite this, melanoma-related deaths, particularly from metastatic

disease, have declined owing to advances in targeted and immune-based therapies[3]. Among the genetic aberrations, *BRAF* mutations are the most prevalent, establishing this gene as a key therapeutic target[6]. Accordingly, *BRAF* inhibitors, such as vemurafenib, dabrafenib, and encorafenib, have demonstrated superior efficacy over conventional chemotherapy[7]. Given its immunogenic nature, melanoma responds favorably to immune modulation[8]; consequently, it has served as the foundation for the clinical development of immunotherapy before its application to other malignancies[9]. Multiple immune checkpoint inhibitors have since gained FDA approval, revolutionizing advanced melanoma treatment and increasing the 5-year relative survival rate to approximately 44%[10]. However, resistance to both targeted and immune therapies remains a major clinical challenge[11].

Although *BRAF* inhibitors yield improved outcomes, treatment failure commonly arises from acquired resistance via MAPK pathway reactivation and MEK signaling[7]. This led to the development of combined *BRAF* and MEK inhibitor regimens, which are now approved in three formulations for melanoma, although they are associated with adverse events in 45-70% of patients[7]. In 2015, the FDA approved the ipilimumab-nivolumab combination, achieving a 57.6% response rate compared with 43.7% for nivolumab and 19% for ipilimumab alone[7,12]. Nevertheless, approximately 40% of patients with metastatic melanoma remain non-responsive due to primary or acquired resistance[12,13]. Recently, triplet therapy integrating targeted and immune-based agents has shown durable responses without substantial improvement in overall efficacy[7]. Only one such regimen, atezolizumab with cobimetinib and vemurafenib, has received FDA approval (2020) for unresectable $BRAF_{V600E}$ melanoma[14,15]. Despite enhanced therapeutic effects, response rates remain comparable, with 79% of patients experiencing grade 3/4 adverse events and therapy discontinuation in 13%[16].

Recent evidence indicates that dysregulated epigenetic mechanisms contribute to therapeutic resistance to both targeted therapies and immunotherapies in various cancers, including melanoma[17,18]. This has prompted the development of small-molecule inhibitors targeting key epigenetic regulators, several of which have shown promising activity in preclinical and clinical studies[19]. Among these, enhancer of zeste homolog 2 (EZH2), the catalytic subunit of the polycomb repressive complex 2 (PRC2), acts as a master regulator of gene expression and is associated with drug resistance and immune modulation in multiple cancers[20]. Consequently,

EZH2 has emerged as a potential therapeutic target in diverse tumor types[21], leading to the FDA approval of the first EZH2 inhibitor, tazemetostat, in June 2020 for relapsed or refractory follicular lymphoma[22,23]. In melanoma, *BRAF*$_{V600E}$ driven signaling upregulates EZH2 expression, which correlates with poorer survival[24]. Moreover, EZH2 dysregulation alters regulatory T-cell function, thereby suppressing antitumor immunity[25]. Although several EZH2 inhibitors are under investigation, no monotherapy has demonstrated meaningful clinical efficacy in melanoma[17]. Approved agents, such as tazemetostat, exhibit limited activity and fail to enhance immune-mediated tumor clearance in melanoma[26,27]. Despite being generally well tolerated, tazemetostat can induce adverse effects that may constrain its utility, particularly in combination regimens[28,29]. Collectively, these findings underscore the need for newer EZH2 targeted therapies with improved efficacy and safety profiles to overcome therapeutic resistance in melanoma.

Phytochemicals are naturally occurring bioactive compounds in plants that have significantly contributed to the development of modern cancer therapeutics[30]. In addition to their anticancer efficacy, their low toxicity, cost-effectiveness, and widespread availability make them promising candidates for cancer treatment[31,32]. *Taxus baccata*, a species of the *Taxus* genus, holds considerable value in traditional medicine across various cultures due to its broad pharmacological activities. In Ayurveda and Unani systems, *Taxus* species are used to manage common cold symptoms and reduce inflammation. Members of the *Taxus* genus are well-documented for their tumor-suppressive potential[33]. Paclitaxel (Taxol), isolated from the bark of *Taxus* trees, is an FDA-approved chemotherapeutic agent widely used against various malignancies[34,35]. Accordingly, the present study employed computational approaches to investigate *T. baccata*-derived phytochemicals as potential inhibitors of EZH2, with the aim of identifying effective candidates for the treatment of therapy-resistant melanoma.

2. Methodology

2.1 Retrieval and preparation of ligand library

The PubChem Compound Identifiers (CIDs) of all bioactive metabolites of *Taxus baccata* were retrieved from the Indian Medicinal Plants, Phytochemistry, and Therapeutics (IMPPAT) database (https://cb.imsc.res.in/imppat/), which encompasses 4,010 Indian medicinal plants and 17,967 phytochemicals[36]. After removing duplicates, 98 unique phytochemicals were selected for further

analysis (Supplementary Table 1). Two compounds, tazemetostat (CID: 66558664) and GSK126 (CID: 68210102), were used as control drugs. Tazemetostat is currently the only FDA-approved EZH2 inhibitor[37], while GSK126 was chosen based on its reported preclinical efficacy in combination with vemurafenib against melanoma[17]. The three-dimensional (3D) structures of all ligands were retrieved from the PubChem database (https://pubchem.ncbi.nlm.nih.gov/) in SDF format[38,39]. The structures were optimized using Gaussian 09 with Density Functional Theory (B3LYP/6-311G(d,p)) under gas-phase conditions[40,41]. Subsequently, Open Babel (https://sourceforge.net/projects/openbabel/) was employed to construct the ligand library[5], and the compounds were energy-minimized using the Universal Force Field (UFF) with the Conjugate Gradient algorithm implemented in PyRx[42].

(**Supplementary Table 1**: General information of the ligand library)

2.2 Protein preparation, validation, and active site prediction

The three-dimensional (3D) structure of EZH2 (PDB ID: 4MI5, 2.00 Å resolution) was retrieved from the RCSB Protein Data Bank (https://www.rcsb.org/structure/4MI5). The protein was prepared in Discovery Studio 2024 (https://discover.3ds.com/discovery-studio-visualizer-download) by removing the bound cofactors, water molecules, and metal ions, followed by energy minimization using the Swiss PDB Viewer (https://spdbv.vital-it.ch/) to stabilize the structure[43]. The quality of the structure was validated using SAVES v6.1 (https://saves.mbi.ucla.edu/) employing ERRAT, VERIFY and PROCHECK programs[44], MolProbity (https://molprobity.biochem.duke.edu/),and ProSA-Web (https://prosa.services.came.sbg.ac.at/prosa.php)[45] to ensure structural reliability. Ligand-binding pockets were subsequently identified using the CASTpFold (https://cfold.bme.uic.edu/castpfold/) server, which detects surface pockets and internal cavities based on computational geometry[46,47]. The draggability of the predicted pockets was further analyzed using the PockDrug server (https://pockdrug.rpbs.univ-paris-diderot.fr)[48].

2.3 Molecular docking and interaction analysis

A total of 100 compounds, including phytochemicals and controls, were subjected to molecular docking using PyRx v0.8, which integrates AutoDock Vina (v1.2.0) for virtual screening[42,49]. The grid box dimensions were defined based on the predicted active sites obtained from the

CASTpFold and PockDrug servers. All the docking parameters were maintained at the default settings. The docking results were ranked according to the binding affinity (kcal/mol), where lower (more negative) values indicated stronger binding[50]. Top-scoring compounds exhibiting higher binding affinities than both controls were shortlisted. The protein–ligand interactions of the shortlisted compounds and controls were further analyzed and visualized in two dimensions using BIOVIA Discovery Studio Visualizer, focusing on hydrogen bonds, hydrophobic interactions, and interacting residues. The three-dimensional binding conformations of the docked complexes were visualized using PyMOL v4.6.0[51].

2.4 Pharmacological and toxicological profiling

An in silico computational approach was employed to evaluate the physiological, pharmacological, and toxicological properties of the shortlisted compounds and controls. Drug-likeness, medicinal chemistry parameters, and key physicochemical properties, including molecular weight, lipophilicity, and water solubility, were assessed using the SwissADME web tool (https://www.swissadme.ch/)[52]. The pharmacokinetic properties, including Absorption, Distribution, Metabolism, and Excretion (ADME), were predicted using the pkCSM platform (https://biosig.lab.uq.edu.au/pkcsm/)[53]. Toxicity profiles were evaluated using the ADMETlab 2.0 (https://admetmesh.scbdd.com/) and ProTox 3.0 (https://tox.charite.de/protox3/) web servers[54–56]. To estimate the potential antineoplastic activities based on the structural and physicochemical features of the compounds, predictions were performed using the PASS Online (https://way2drug.com/PassOnline/) web server. A probability value of Pa > Pi indicates a higher likelihood of the compound exhibiting a specific biological activity[57]. Furthermore, cytotoxicity against tumor and non-tumor melanoma cell lines was predicted using the CLC-Pred 2.0 server (https://way2drug.com/clc-pred/), which applies a naïve Bayes classifier to estimate cytotoxic potential, with values ranging from 0.000 to 1.000, representing the likelihood of cell death or damage[58].

2.5 Quantum mechanical (QM) calculation

Density Functional Theory (DFT) was employed to perform quantum mechanical calculations on the shortlisted compounds following molecular docking and subsequent in silico analyses. The analysis was performed using Gaussian 9 employing the DFT/B3LYP/6–311G (d,p) method[40].

Previous studies have demonstrated that the DFT/B3LYP/6–311G (d,p) theoretical framework is accurate and effective[41,59]. The compounds were studied to determine how they accept and donate electrons by calculating the energies of their frontier molecular orbitals, specifically the highest occupied molecular orbital (HOMO) and the lowest unoccupied molecular orbital (LUMO), as well as the energy gap and molecular electrostatic potential, using the GaussView 5 software. These features also convey information about the chemical reactivity and stability of the substances[59,60]. The following equations were used for the calculations:

$$E_{gap} = (E_{LUMO} - E_{HOMO})\ ;\ I = -E_{LUMO}\ ;\ A = -E_{HOMO};$$

$$\mu = -\frac{(I + A)}{2}\ ;\ \chi = \frac{(I + A)}{2}\ ;\ \varpi^2 = \frac{\mu^2}{2\eta}\ ;\ \eta = \frac{I - A}{2}\ ;\sigma = \frac{1}{\eta}$$

where, E_{gap} is the energy gap, E_{LUMO} is the lowest unoccupied molecular orbital, E_{HOMO} is the highest occupied molecular orbital, I is the ionization potential, A is the electron affinity, μ is the chemical potential, χ is the electronegativity, ϖ is the electrophilicity, η is the chemical hardness and σ is the chemical softness.

2.6 Molecular dynamics simulation and post-simulation analysis

Molecular dynamics (MD) simulations were conducted to investigate the structural stability of the protein-ligand complexes obtained from molecular docking. Simulations were performed using YASARA Structure (Product name: YASARA Dynamics) (http://www.yasara.org/products) for 100 ns for both ligand and control systems. Homology modeling was performed using a multi-step procedure in YASARA, during which the modeling parameters and targets were defined according to the macro instructions[61]. The equilibrated systems were subsequently subjected to MD simulations using the default YASARA Structure MD macro settings (http://www.yasara.org/md_run.mcr)[62]. All simulations were carried out with the AMBER force field under standard conditions: temperature of 298 K, pressure of 1 bar, a 7.86 Å Coulomb cut-off, 0.9% NaCl for charge neutralization, solvent density of 0.997 g/cm³, pH 7.0, 1 fs time steps, periodic boundary conditions, and all atoms set as mobile[61,63]. Post-simulation analyses included the calculation of the interaction energy, root mean square deviation (RMSD), root mean square fluctuation (RMSF), radius of gyration (Rg), solvent-accessible surface area (SASA), and total number of hydrogen bonds from the generated trajectory files

2.7 MM-PBSA analysis

The Molecular Mechanics Poisson-Boltzmann Surface Area (MM-PBSA) method was employed to estimate the binding free energy of the protein-ligand complexes. The binding free energy was calculated using the following equation[64]:

$$\Delta G_{Binding} = G_{Complex} - \left(G_{Protein} + G_{Ligand}\right)$$

where $\Delta G_{Binding}$ represents the total binding free energy, $G_{Complex}$ denotes the total free energy of the protein-ligand complex, and $G_{Protein}$ and G_{Ligand} correspond to the total free energies of the unbound protein and ligand, respectively[63]. Snapshots extracted from the 100 ns MD simulation were analyzed using the MM-PBSA method implemented in the YASARA Structure (YASARA Biosciences) simulator[65]. MM-PBSA provides a robust post-simulation rescoring approach that yields more accurate estimates of binding affinities than conventional docking scoring functions.

2.8 Principal component analysis (PCA)

Principal component analysis was used to explore the predominant dynamic molecular motions during the MD simulation period. The covariance matrix classifies the molecular atomic motions[66]. The simulation trajectory data were obtained from YASARA, and to explain the differences between the groups, several structural and energy data, including bond lengths, bond angles, dihedral angles, planarity, van der Waals energies, and electrostatic energies, were considered for each trajectory[67]. . Based on these datasets the plots were projected using ggplot2 library from R (version 4.5.1)[68].

3. Results

3.1 Protein validation

The structural quality of the selected protein (PDB ID: 4MI5) was validated using multiple approaches. VERIFY 3D analysis showed that 48.08% of residues had an average 3D–1D score ≥ 0.1, and ERRAT reported an overall quality factor of 95.7447, indicating good model reliability.

Ramachandran plot analysis using PROCHECK and MolProbity revealed only one residue in the disallowed region (Figure 1 A and B), confirming proper stereochemical geometry. Other data are included in the Supplementary Table 2. ProSA-Web analysis yielded a Z-score of -5.32, consistent with native proteins of similar size (Figure 1 C). The energy profile indicated predominantly low-energy residues, suggesting well-defined regions, with a few central residues showing positive values, aligning with the ERRAT findings (Supplementary Figure 1).

(**Supplementary Figure 1**: Histogram showing protein-model validation errors. Yellow bars indicate outlier regions exceeding quality thresholds; white bars represent acceptable error levels within the structural validation range.)

(S**upplementary Table 2:** Ramachandran quality parameters for 4MI5)

(**Figure 1** Protein validation plots. (A) PROCHECK Ramachandran plot, (B) MolProbity Ramachandran plot, (C) ProSA-Web Z-score, and (D) ProSA-Web local quality profile)

3.2 Active site prediction and grid box generation

The Computed Atlas of Surface Topography of the universe of protein Folds (CASTp) server was used to predict potential ligand-binding pockets in the target protein. Among the 24 identified cavities, the top three pockets ranked by solvent-accessible volume and area were considered, while smaller pockets were excluded because of ligand size constraints[69,70]. Pocket druggability was assessed using PockDrug, where a probability ≥ 0.50 indicates a "druggable" site[48]. Three pockets met these criteria. Visualization in PyMOL indicated that CastpFold pockets 1 and 3 were the most plausible binding sites, based on their larger volume, area, and overlap with highly druggable residues. A grid box encompassing both pockets was defined (dimensions: X = 35.661 Å, Y = 36.019 Å, Z = 25.328 Å; center: X = 29.358, Y = 26.240, Z = 3.131) to ensure the coverage of potential alternative binding sites. All results are depicted in Figure 2.

(**Figure 2:** Active site prediction and grid generation. (A) Top 3 pockets predicted by CASTpFold, (B) Top 3 druggable pockets predicted by PockDrug, and (C) Grid box parameters with surface representation of the target region.)

3.3 Molecular docking analysis

Among the 98 screened phytochemicals (Supplementary Table 3), four compounds demonstrated higher binding affinities than the control ligands against the target protein. Sotetsuflavone (CID: 5494868) exhibited the highest docking score (-10.4 kcal/mol), surpassing the control compounds tazemetostat (CID: 66558664) and GSK126 (CID: 68210102), which showed docking scores of -9.2 and -8.9 kcal/mol, respectively (Figure 3). sequoiaflavone (CID: 5484010) and di-o-methyl amentoflavone (CID: 5491518) displayed docking scores comparable to those of tazemetostat (CID: 66558664); however, they were excluded from further consideration because the selection criteria were restricted to compounds with higher binding affinities than those of both controls. Consequently, the top four phytochemicals, along with the two controls, were selected for further analysis.

(**Supplementary Table 3**: Binding affinities of *T. baccata*-derived phytochemicals)

(Figure 3: Docking scores (kcal/mol) of top *T. baccata* compounds compared with control ligands. Negative values above each bar denote the binding affinities. Tazemetostat and GSK126 served as controls.)

3.4 Protein-ligand interaction analysis

The molecular interactions between the shortlisted ligands and control compounds are illustrated in Figure 4. Various noncovalent interactions, including conventional hydrogen bonds, carbon hydrogen bonds, π-donor hydrogen bonds, and π-alkyl and π-sigma interactions, were observed. Sotetsuflavone (CID: 5494868) and ginkgetin (CID: 5271805) formed the highest number of hydrogen bonds (seven each) with the target proteins. Sotetsuflavone (CID: 5494868) interacted with SER524 (2.20 Å), LEU525 (2.74 Å), GLN526 (2.61 Å), ASN546 (2.71 Å), ALA581 (1.87 Å), ASN675 (2.55 Å), and GLN735 (2.41 Å). Ginkgetin (CID: 5271805) exhibited similar interactions with SER524 (2.32 Å), LEU525 (2.76 Å), ASN546 (2.03 Å), PHE547 (2.29 Å), ALA581 (2.43 Å), ASN675 (2.46 Å), and GLN735 (2.82 Å). Both compounds formed π-donor hydrogen bonds with LEU525 and additional π interactions with other residues (Supplementary Table 4). amentoflavone (CID: 5281600) formed hydrogen bonds with SER524 (3.72 Å), GLN526

(2.42 Å), ALA581 (1.83 Å), and VAL704 (2.99 Å), and the interaction with SER524 involved a carbon–hydrogen bond. Additional π–π interactions were observed with ALA581, VAL582, VAL704, MET706, and HIS711 (Supplementary Table 4). Podocarpusflavone A (CID: 5320644) and the control ligands formed two hydrogen bonds each and displayed multiple π–π and alkyl interactions with various residues (Supplementary Table 4).

(Supplementary Table 4: Non-Bond interactions of selected ligands and the controls)

(Figure 4*:* Structural representation of shortlisted ligands and control compounds bound to the target protein active site. The left panel of each image depicts the 3D surface view of the ligand within the protein's active site, while the right panel illustrates the corresponding 2D protein-ligand interaction map.)

3.5 Pharmacological and toxicological profiling

3.5.1 Physicochemical properties and drug likeliness prediction

The drug-likeness of the shortlisted phytochemicals and reference inhibitors was evaluated based on Lipinski's rule of five, using the SwissADME web server. Lipinski's criteria stipulate that an orally active compound should not violate more than one of the following parameters: hydrogen bond donors ≤ 5, hydrogen bond acceptors ≤ 10, molecular weight < 500 Da, and Log $P_{o/w}$ ≤ 5. All shortlisted ligands, except amentoflavone (CID: 5281600), complied with these criteria, with at most one violation. Compared to the reference inhibitors, all phytochemicals displayed higher topological polar surface area (TPSA) values than the reference inhibitors. In addition, the phytochemicals exhibited lower lipophilicity values than the control compounds. However, all tested compounds, including the controls, demonstrated poor water solubility; notably, ginkgetin (CID: 5271805) was predicted to be insoluble. The bioavailability scores and pan-assay interference compound (PAINS) alerts were identical across all tested molecules, indicating the absence of structural red flags for assay interference. Furthermore, synthetic accessibility scores suggested that all phytochemicals were easier to synthesize than GSK126 (CID: 68210102). Among the phytochemicals, only ginkgetin (CID: 5271805) showed a slightly higher synthetic complexity than tazemetostat (CID: 66558664). All results are summarized in Tables 1 and 2.

(Table 1: Physicochemical property evaluation of the shortlisted phytochemicals and reference inhibitors.)

(Table 2: Drug-likeness and medicinal chemistry profile of the shortlisted phytochemicals and reference inhibitors.)

3.5.2 Assessment of pharmacokinetic properties

The predicted pharmacokinetic parameters of the shortlisted phytochemicals and controls are summarized in Table 3. All six compounds exhibited favorable intestinal absorption. Ginkgetin (CID: 5271805) demonstrated the highest predicted absorption (95%), whereas both controls showed comparable absorption values (≈ 91%). Podocarpusflavone A (CID: 5320644) exhibited the lowest absorption (79%), while except for ginkgetin (CID: 5271805), all compounds were identified as substrates of P-glycoprotein (P-gp), indicating a higher likelihood of efflux from the intestinal epithelium. Notably, sotetsuflavone (CID: 5494868) was the only compound not classified as a P-gp inhibitor I, suggesting a reduced potential for efflux-mediated interactions and a lower risk of drug-drug interactions (DDIs). However, all six compounds were predicted to act as P-gp inhibitor II. Compared to the controls, all four phytochemicals exhibited lower predicted volume of distribution (Vd), indicating limited tissue penetration, and a lower propensity for blood-brain barrier (BBB) permeation. Metabolic predictions revealed that both controls were substrates of Cytochrome P450 3A4 (CYP3A4) and inhibitors of Cytochrome P450 2C9 (CYP2C9) and CYP3A4, suggesting potential self-inhibition of metabolism. Among the phytochemicals, ginkgetin (CID: 5271805) and podocarpusflavone A (CID: 5320644) were predicted to be CYP3A4 substrates and CYP2C9 inhibitors. In contrast, sotetsuflavone (CID: 5494868) and amentoflavone (CID: 5281600) were predicted as CYP3A4 substrates but showed no inhibitory activity toward major CYP isoforms (CYP1A2, CYP2C19, CYP2C9, CYP2D6, or CYP3A4), indicating potentially safer metabolic profiles. The predicted clearance values for the five compounds fell within a moderate range (0.61-0.86 mL/min/kg), whereas amentoflavone (CID: 5281600) exhibited a slightly lower clearance rate. None of the six compounds were predicted to be substrates of organic cation transporter 2 (OCT2), suggesting a limited role of renal secretion in their elimination.

(Table 3: Evaluation of ADME properties of the selected phytochemicals and the controls.)

3.5.3 Estimation of antineoplastic activities

The antineoplastic potential of the shortlisted phytochemicals was evaluated using the online PASS prediction tool. As summarized in Table 4, all selected ligands exhibited predicted antineoplastic activity against melanoma, whereas none of the controls showed any corresponding predicted values. These findings suggest that the shortlisted compounds may possess therapeutic potential for melanoma treatment by inhibiting tumor cell proliferation and enhancing anti-tumor immune responses. In contrast, the controls showed no predicted antineoplastic activity related to melanoma.

(Table 4: Predicted antineoplastic activity of the selected phytochemicals and the controls against melanoma.)

3.5.4 Toxicological evaluation

The toxicological parameters of the shortlisted compounds and control drugs were assessed using two predictive platforms, ADMETlab 2.0 and ProTox-III, and the results are summarized in Table 5. All shortlisted compounds demonstrated lower rat oral acute toxicity than the controls, indicating a favorable safety margin. While both control compounds showed moderate to high probabilities of hERG channel inhibition, none of the phytochemicals were predicted to be hERG inhibitors. Similarly, although the controls exhibited a high likelihood of hepatotoxicity, none of the shortlisted compounds were predicted to be hepatotoxic, which is a significant observation given the frequent hepatotoxic effects associated with conventional cancer therapies. Except for GSK126 (CID: 68210102), none of the compounds were predicted to be mutagenic. Moreover, the shortlisted compounds exhibited a higher probability of being non-mutagenic than tazemetostat (CID: 66558664).

(Table 5: Predicted toxicological profiles of the shortlisted compounds and controls)

3.5.5 Cell line cytotoxicity prediction

The cytotoxic potential of the compounds was predicted in terms of Pa (probability to be active) and *Pi* (probability to be inactive), which ranged from 0.000 to 1.000. Compounds with Pa > Pi were considered potentially cytotoxic (active) compounds. A Pa value greater than 0.5 indicates high cytotoxic activity, Pa values between 0.3 and 0.5 suggest intermediate activity, and Pa values

< 0.3 indicate low activity[58]. Using CLC-Pred, in silico cytotoxicity predictions were performed for the shortlisted compounds and controls against different melanoma cell lines. No data were available for the control compounds in melanoma cell lines. All shortlisted phytochemicals exhibited intermediate cytotoxic activity against SK-MEL-1 cells, with amentoflavone (CID: 5281600) showing the highest Pa value (0.384). In contrast, their predicted activity against other melanoma cell lines was low (Pa < 0.3). Notably, the predicted cytotoxicity of these compounds toward normal cell lines were lower than those toward malignant cell lines, suggesting a favorable selectivity profile. This indicates that the shortlisted compounds may selectively target malignant cells while sparing normal cells, which is a desirable property for anticancer drug development. The prediction results are presented in Table 6.

Table 6: Predicted cytotoxicity of shortlisted compounds and controls against skin tumor and non-tumor cell lines using CLC-Pred (Pa > Pi).

3.6 DFT calculations

3.6.1 Analysis of thermodynamic properties

The thermodynamic properties of the shortlisted compounds and controls were evaluated using the DFT/B3LYP/6–311G(d,p) level of theory. All investigated phytochemicals exhibited more negative free energy values than the controls (Figure 5 A). Among the six compounds analyzed, GSK 126 (CID: 68210102) displayed the lowest negative free energy, indicating the lowest thermodynamic stability within the group. In contrast, ginkgetin (CID: 5271805) was identified as the most stable compound, exhibiting the highest negative free energy value (-1984.40 Hartree). Furthermore, sotetsuflavone (CID: 5494868) exhibited the lowest dipole moment (1.82 Debye) among the compounds studied (Figure 5 B), suggesting greater intramolecular stability and a lower tendency to interact with polar solvents. Although the remaining shortlisted phytochemicals exhibited higher dipole moments than tazemetostat (CID: 66558664), all of them showed lower values than GSK 126 (CID: 68210102), which had the highest dipole moment (7.44 Debye).

(Figure 5: Thermodynamic properties of the shortlisted compounds from *T. baccata* and the controls. (A) Gibbs free energy values. (B) Dipole moment values)

3.6.2 Frontier molecular orbitals

Frontier molecular orbital (FMO) analysis was performed to evaluate the reactivity and potential reactive sites of the selected compounds. The HOMO and LUMO distributions of the compounds are shown in Figure 6. Compared to the control ligand tazemetostat (CID: 66558664), which exhibited the largest HOMO-LUMO energy gap, all the shortlisted phytochemicals demonstrated lower energy gaps, indicating enhanced chemical reactivity and thermodynamic stability. Although their energy gaps were slightly higher than those of GSK 126 (CID: 68210102), the phytochemicals displayed notably higher HOMO and LUMO energy levels relative to both controls, suggesting a stronger electron-donating and accepting capacity. As summarized in Table 7, these compounds also exhibited lower hardness (η) and higher softness (σ) values than tazemetostat (CID: 66558664), implying a greater ability to redistribute electron density upon interaction with the protein environment. This property is particularly advantageous for stable binding within the polar and tightly packed pockets of target proteins.

(**Figure 6**: Frontier molecular orbitals (HOMO-LUMO) and energy gaps of the shortlisted phytochemicals and controls. Depicted are the HOMO and LUMO distributions with respective energy gap (ΔE) values, representing the electronic properties and stability of each compound.)

(Table 7: Calculated frontier molecular orbital (FMO) energies and associated global reactivity descriptors.)

3.6.3 Molecular electrostatic potentials

To identify the reactive regions of the shortlisted phytochemicals and control compounds, their three-dimensional charge distributions were analyzed using molecular electrostatic potential (MEP) mapping, as shown in Figure 7. The electrostatic potential values ranged from +6.470 to +8.007 a.u. for the most positive regions and from −6.470 to −8.007 a.u. for the most negative regions. Among the analyzed compounds, sotetsuflavone (CID: 5494868) exhibited the most negative potential (−8.007 a.u.), indicating a strongly electron-rich region with a high propensity for hydrogen bond acceptance. Podocarpusflavone A (CID: 5320644) showed the second most negative potential (−7.824 a.u.), followed by ginkgetin (CID: 5271805) (−7.821 a.u.). In contrast, the control compound tazemetostat (CID: 66558664) displayed the least negative potential (-6.470

a.u.), suggesting a comparatively weaker electron density pocket and lower hydrogen bond-accepting capability.

(**Figure 7**: Molecular electrostatic potential (MEP) maps of shortlisted compounds from T. baccata. The MEP maps illustrate the charge distribution across each molecule: blue indicates regions of positive potential (low electron density), red denotes negative potential (high electron density)).

3.7 Molecular dynamics (MD) simulation analysis

The structural and interaction stability of protein ligands can be predicted using MD simulations, which also aids in validating post-docking analysis. The four lead compounds, along with two controls, tazemetostat (CID: 66558664) and GSK126 (CID: 682101020), underwent MD simulations for 100 ns. The trajectory data and interaction pose obtained from MD simulations were analyzed using several computational metrics, such as the root mean square deviation (RMSD), root mean square fluctuations (RMSF), radius of gyration (Rg), and solvent-accessible surface area (SASA), to investigate the structural stabilities. In addition to the hydrogen bond analysis, the post-simulation MM-PBSA was analyzed for interaction stabilities. Subsequently, DCCM and PCA analyses were performed using data obtained from the MD simulation, and the graphs were projected using the ggplot2 library in R. Further, a statistical analysis was conducted to measure the standard deviation (SD) to evaluate the analytical and statistical relevance of the procedure.

(Table 8: The average values with standard deviations (SD) of RMSD, RMSF, RoG, SASA, H-bonds, and MM-PBSA-based binding free energy (ΔG) for all protein–ligand complexes)

3.7.1 Root mean square deviation (RMSD) analysis

To gain a better understanding of the dynamic behavior and stability of the protein–ligand complex, the results of the MD simulations for both the controls and ligand complexes were analyzed for each trajectory, and the RMSD values were plotted and projected (Figure 8A). The RMSD provides insight into the extent to which a group of atoms deviates from the original reference structure of a protein, ligand, or ligand-protein complex. A substantial amount of stability or instability related to the conformational changes of the molecule can be correlated with

RMSD values. The average RMSD values for the sotetsuflavone (CID: 5494868), ginkgetin (CID: 5271805), amentoflavone (CID: 5281600), podocarpusflavone A (CID: 5320644), tazemetostat (CID: 66558664), and GSK 126 (CID: 68210102) were 2.84 Å, 4.67 Å, 3.27 Å, 3.55 Å, 3.8 Å, and 3.21 Å, respectively. The RMSD of ginkgetin (CID: 5271805) gradually increased and exhibited relatively higher fluctuations among all of them, notably increasing progressively after 55 ns, after which the value reached a maximum and remained constant until the end of the MD simulation. In contrast, the sotetsuflavone (CID: 5494868) complex exhibited the lowest average score with negligible fluctuations, and its highest peak occurred at approximately 5 and 20 ns, indicating a highly stable conformation among all the complexes. A comparable deviation pattern was observed for podocarpusflavone A (CID: 5320644) and amentoflavone (CID: 5281600) during the simulation period. However, the tazemetostat (CID: 66558664) complex exhibited relatively higher RMSD values during the 57-88 ns and 34-45 ns intervals than the podocarpus flavone A (CID: 5320644) complex. Similarly, amentoflavone (CID: 5281600) overlapped with GSK 126 (CID: 68210102) for most of the study period, and the average value was very close to that of the control.

3.7.2 Root mean square fluctuation (RMSF)

The RMSF values were plotted to evaluate the residue-wise fluctuations between the protein and ligand complexes. To understand the residues that contribute to the causative factors of fluctuations, the RMSF plot is provided in (Figure 8 B). The RMSF value was used to identify the rigid and flexible regions of the protein. This validation criterion for structural variability in the ligand-protein complex highlights the importance of specific protein residues in these structural shifts. Using a timescale of 100 ns, the amino acid deviation value was calculated for each position. As illustrated in Figure 8(B), the average RMSF values for sotetsuflavone (CID: 5494868), ginkgetin (CID: 5271805), amentoflavone (CID: 5281600), podocarpusflavone A (CID: 5320644), tazemetostat (CID: 66558664), and GSK 126 (CID: 68210102) were 1.72 Å, 2.88 Å, 2.15 Å, 1.96 Å, 2.32 Å and 2.06 Å respectively. When comparing the values of the control RMSFs to those of the protein-ligand complex RMSFs, it was observed that sotetsuflavone (CID: 5494868) and amentoflavone (CID: 5281600) demonstrated greater fluctuations than both control complexes. Here, ginkgetin (CID: 5271805) exhibited relatively higher residue fluctuations, particularly near the N-terminal region, reaching a value of approximately 12.5 Å, suggesting that higher RMSF

values are indicative of a more flexible protein structure. For podocarpusflavone A (CID: 5320644), the amino acid position from 135 to 140 exhibited a deviation of up to 8.5 Å, whereas the maximum amino acids exhibited fluctuations of 1–5 Å. Similarly, another sotetsuflavone (CID: 5494868) also exhibited fluctuations in the same regions, confirming that both compounds had lower RMSF values than the controls in the RMSF plot.

(**Figure 8**: Molecular Dynamic Simulation Analysis Structural Stability (100 ns) (A) Root-mean-square deviation (RMSD) (B) Root-mean-square fluctuation (RMSF) (C) Radius of gyration (Rg) analysis (D) Solvent accessible surface area (SASA))

3.7.3 Radius of gyration (Rg) analysis

Throughout the simulation, Rg parameter determines the compactness of a structure. An increase in the Rg values suggests a reduction in the compactness of the protein structure, indicating increased flexibility and decreased stability. The Rg-time fluctuations were observed to be nearly constant within the range of 18.7-19.5 Å, indicating that the protein-ligand complexes undergo stable conformational changes. As shown in (Figure 8 C), the average Rg values for the sotetsuflavone (CID: 5494868), ginkgetin (CID: 5271805), amentoflavone (CID: 5281600), podocarpusflavone A (CID: 5320644), tazemetostat (CID: 66558664), and GSK 126 (CID: 68210102) were 18.96 Å 19.36 Å, 18.88 Å, 18.87 Å, 19.36 and 19.13 Å, respectively. Among these, podocarpusflavone A (CID: 5320644) exhibited the lowest average Rg value, suggesting the highest degree of compactness and conformational stability of the ligand. Compared to ginkgetin (CID: 5271805) and sotetsuflavone (CID: 5494868), the radius of gyration was the smallest for the amentoflavone (CID: 5281600) complex (Figure 8 C). Significant fluctuations were observed in the tazemetostat (CID: 66558664) and ginkgetin (CID: 5271805) complexes at approximately 18-33 ns; however, the systems quickly regained stability for the remainder of the time, with a similar average score. Therefore, the podocarpusflavone A (CID: 5320644) complex maintained a higher degree of stability during the simulation and successfully bound to the ligand.

3.7.4 Solvent accessible surface area (SASA) analysis

The information obtained from SASA will help determine whether the ligand is retained within the shallow binding pocket or expelled from the binding cavity. A high SASA value indicates a greater residue exposure to water, reflecting a larger binding interface. The average SASA values

of the protein-ligand complex are 12102.7 Å², 11786.5 Å², 11929.2 Å², 11896.7 Å², 12134.5 Å², and 12352.5 Å² for the compounds ginkgetin (CID: 5271805), amentoflavone (CID: 5281600), podocarpusflavone A (CID: 5320644), sotetsuflavone (CID: 5494868), tazemetostat (CID: 66558664), and GSK 126 (CID: 68210102), respectively, as illustrated in (Figure 8 D). amentoflavone (CID: 5281600) exhibited the lowest average SASA, indicating that it was more deeply embedded within the protein's binding pocket in the complex system, thereby enhancing its effectiveness in modulating the biological activity of the target. It has been shown that all the lead complexes display comparatively lower SASA scores compared to the controls.

3.7.5 Hydrogen bond analysis

Hydrogen bonds are a type of non-covalent conventional interaction that is crucial for binding ligands appropriately in the active sites as well as biological processes. The biomolecular and biochemical regulation of a ligand relies on the formation of hydrogen bonds[71]. Hydrogen bond interactions between the lead complexes and controls were analyzed during the molecular dynamics simulation. Every compound formed numerous hydrogen bonds concurrently, with several hydrogen bonds ranging from 390 to 460, as shown in (Figure 9 A**)**. These six compounds, sotetsuflavone (CID: 5494868), ginkgetin (CID: 5271805), amentoflavone (CID: 5281600), podocarpusflavone A (CID: 5320644), tazemetostat (CID: 66558664), and GSK 126 (CID: 68210102), had average hydrogen bond numbers of 422.73, 430.57, 424.59, 429.24, 424.53 and 422.92 respectively. Among the studied complexes, ginkgetin (CID: 5271805) and Amentoflavone (CID 5281600) exhibited slightly higher H-bond counts than the other complexes; therefore, these ligands are expected to have better interaction stabilities and will show favorable regulation of biological processes.

3.7.6 Binding free energy estimation MMPBSA

The binding free energy (ΔG_{Bind}) of the protein-ligand complexes was estimated using the Molecular Mechanics/Poisson-Boltzmann Surface area (MM/PBSA) approach to evaluate the protein–ligand complex interaction stability and binding affinity. However, a lower binding energy value indicates stronger interactions between the ligand and protein, suggesting a more stable complex. Among all the complexes analyzed, compound amentoflavone (CID: 5281600) exhibited the most favorable binding energy (−101.73 kJ/mol), followed by GSK 126 (CID: 68210102) (−67.77 kJ/mol), sotetsuflavone (CID: 5494868) (−67.53 kJ/mol), and podocarpusflavone A (CID:

5320644) (−45.32 kJ/mol) (Figure 9 B). In contrast, ginkgetin (CID: 5271805) displayed a comparatively weaker binding affinity (−16.07 kJ/mol), whereas the reference inhibitor tazemetostat (CID: 66558664) showed a positive energy value (+7.38 kJ/mol), suggesting lower stability relative to the ligands. The consistent negative free energy values for most complexes throughout the simulation period reflected stable binding interactions within the active pocket. Overall, the MM/PBSA analysis confirmed that amentoflavone (CID: 5281600) formed the most thermodynamically favorable and stable complex with the target protein compared to the controls and other ligands.

(**Figure 9**: Molecular Dynamic Simulation Interaction Stabilities (100 ns). (A) Hydrogen bond analysis (B) Binding free energy MMPBSA)

3.7.7 Principal Component Analysis

Principal component analysis (PCA) was performed to evaluate and compare the collective motions and fluctuations within the protein-ligand complexes during molecular dynamics (MD) simulations. Approximately 90% of the total variance was accounted for by the first three principal components, with PC-1 contributing 62%. The predominant eigenvectors associated with PC-1 were Coulomb, van der Waals (VdW), bond, and angle, representing large-scale collective structural motions and electrostatic fluctuations. Dihedral was the primary eigenvector for PC-2, reflecting the torsional motions of compound backbones and local flexibility, whereas PC-3 was associated with planarity, which implies twisting or flattening of planar molecular regions. The PC1-PC2 and PC1-PC3 scatter plots displayed compact vertical clustering, with minimal variation, indicating high structural stability and similar dynamic behavior across all complexes throughout the simulation. The minimal dispersion of PC-2 and PC-3 suggests that torsional and planar motions contributed only minor variations, without major deviations in the overall conformation. The opposite loadings of Coulomb (+ 0.502) and VdW (− 0.493) in PC-1 indicate an anticorrelation between electrostatic and dispersion interactions, implying a counterbalance between the forces and stability within the binding pocket. In contrast, a broad dispersion was observed in the PC2-PC3 scatter plot, where early trajectory frames (blue-purple) were separated from later ones (red-yellow), suggesting time-dependent conformational transitions, such as torsional rotation and planar twisting, such as ring flipping and side-chain reorientation during ligand binding. The overall PCA results indicated that all six protein-ligand complexes displayed

similar dynamic behaviors and maintained conformational stability throughout the simulation, with limited but notable local flexibility, which may contribute to ligand adaptability within the binding site.

(**Figure 10**: Principal Component Analysis (PCA) of six complexes from 100 ns molecular dynamics simulations The PCA plots depict the structural dynamics and conformational variability of the six protein–ligand complexes over the 100 ns simulation, highlighting dominant motions and collective fluctuations in each system.)

3.7.8 Dynamic Cross-Correlation Matrix (DCCM)

The Dynamic Cross-Correlation Matrix (DCCM) was analyzed to further explore the dynamic behavior of amino acid residues within the EZH2 protein in the presence of the six ligands. It provides insights into the collective motions of the amino acid residues, which play a major role in the interactions. A positive correlation means that the motion of the residues is in the same direction, which reflects domain-level motions, whereas a negative correlation means the opposite direction of motion, which may be linked to allosteric site communications that result in conformational transition.[1] The correlation coefficient ranges from −1 (anticorrelated motion, reddish orange) to +1 (correlated motion, dark blue), where uncorrelated or independent movements are shown by faded green regions amentoflavone (CID: 5281600) exhibited the strongest correlation and off-diagonal correlation, accompanied by moderate anticorrelation, suggesting an overall stable and dynamic interplay of structural residues. Sotetsuflavone (CID: 5494868)**,** GSK 126 (CID: 68210102), tazemetostat (CID: 66558664)**,** and podocarpusflavone A (CID: 5320644) also showed moderate to high levels of correlation with smaller areas of anti-correlation and uncorrelation, indicating stable and internally consistent dynamics with only mild conformational changes. amentoflavone (CID: 5281600) exhibited the strongest correlation and off-diagonal correlation, accompanied by moderate anti-correlation, which suggests an overall stable and dynamic interplay of structural residues. The least amount of anti-correlation was observed for podocarpusflavone A (CID: 5320644)**.** In contrast, the large correlated-anticorrelated domains displayed by ginkgetin (CID: 5271805) indicate opposing motions between protein domains, suggesting possible destabilization.

(**Figure 11:** Dynamic Cross-Correlation Matrix (DCCM) analysis of protein-ligand complexes from 100 ns molecular dynamics simulations. The DCCM plots illustrate correlated and anti-

correlated atomic motions within the protein structures over 100 ns, revealing regions of concerted dynamics and functional connectivity in each complex.)

4. Discussion

Despite major advances in targeted and immunotherapies, most patients with melanoma ultimately relapse, highlighting the urgent need for novel treatment strategies[7]. Emerging evidence implicates aberrant epigenetic modifications in therapeutic resistance, driving interest in epigenetic-targeted interventions[72]. Among these, histone modifications critically regulate gene expression and tumor behavior[18,73]. Enhancer of zeste homolog 2 (EZH2), the catalytic subunit of polycomb repressor complex 2 (PRC2), mediates H3K27me3, silencing tumor suppressor and immune-related genes such as HLA class I and II[17]. EZH2 shares upstream signaling with $BRAF_{V600E}$ and has been linked to drug resistance in melanoma, making it a promising therapeutic target[17,74]. Phytochemicals, with their diverse pharmacological properties, low toxicity, and cost-effectiveness, have shown potential in overcoming drug resistance[75–77]. In this context, phytochemicals derived from *Taxus baccata* were computationally evaluated for their potential to target EZH2 and counter melanoma-therapy resistance.

The selected EZH2 structure (PDB ID: 4MI5) was validated using several quality assessment tools. Although it did not meet the VERIFY score threshold (≥80% residues with a 3D-1D score ≥0.1), it was accepted because this parameter has been reported to perform poorly for crystallized structures[78]. Overall, the combined quality metrics indicated that the structure was suitable for further computational analyses. Subsequently, the ligand-binding sites of the protein structure were predicted using the CASTpFold server, and the druggability of these pockets was evaluated using PockDrug. The identified pockets encompassed both regulatory regions (CXC domain and post-SET) and the primary catalytic SET core, thereby covering potential active and allosteric sites[79]. Molecular docking was performed using a grid box encompassing these pockets, facilitating the design of potential inhibitors capable of simultaneously disrupting the catalytic activity and structural activation of EZH2[79–82]. Furthermore, targeting both regulatory and catalytic regions is expected to reduce the likelihood of diminished efficacy due to single resistance-conferring mutations within the SET core[83]. Following molecular docking of 98 phytochemicals, four candidates demonstrated higher binding affinities toward the target protein than the control compounds. The protein-ligand interactions of these candidates were further analyzed using

molecular docking. Among the docked ligands, sotetsuflavone (CID: 5494868) exhibited the highest docking score (−10.4 kcal/mol), followed by ginkgetin (CID: 5271805) with a binding affinity of − 9.9 kcal/mol. Hydrogen bonds (HBs) are the most prevalent non-covalent interactions in biological systems and play a crucial role in determining the protein-ligand binding affinity and selectivity[84]. Both phytochemicals formed a favorable number of hydrogen bonds with residues at the N-terminal region of the SET domain while predominantly engaging the C-terminal region through hydrophobic interactions. These observations suggest that they may inhibit EZH2 through an allosteric blockade mechanism by stabilizing the enzyme in an inactive conformation[79]. In contrast, amentoflavone (CID: 5281600) and podocarpusflavone A (CID: 5320644) displayed relatively lower docking scores and fewer hydrogen bonds with the target protein in these regions. The advantages of allosteric modulators have been well established[85], as they can overcome the limitations associated with SAM-competitive inhibitors, such as tazemetostat and GSK126, including dependency on SAM competition, reduced inhibition of non-catalytic functions, emergence of resistance through catalytic-site mutations, limited efficacy in certain solid tumor contexts, tumor heterogeneity, and off-target or combination therapy challenges[86–92]]. Consequently, the present findings are particularly significant in the context of these previously reported limitations.

In terms of drug-likeness, amentoflavone (CID: 5281600) did not comply with Lipinski's Rule of Five (Ro5). However, this deviation is acceptable because approximately 49% of FDA-approved oral small-molecule drugs also violate Ro5[93]. Previous studies have similarly reported that many natural products, particularly large and complex flavonoids, retain oral activity despite exceeding the Ro5 thresholds[93]. Pharmacokinetic and toxicological profiling of the top four lead compounds provided valuable insights into their potential efficacy and safety, thereby supporting rational lead selection[94]. Among them, ginkgetin (CID: 5271805) and amentoflavone (CID: 5281600) exhibited the most favorable pharmacokinetic profiles. Ginkgetin (CID: 5271805) showed high predicted intestinal absorption and was not identified as a P-gp substrate, suggesting enhanced oral bioavailability and reduced efflux from cancer cells[95–97]. Nonetheless, it was predicted to function as a P-gp inhibitor, raising the possibility of drug-drug interactions, consistent with prior evidence[98,99]. amentoflavone (CID: 5281600) displayed low predicted clearance (0.484 mL/min/kg) and a minimal CYP inhibition profile, indicating the potential for prolonged systemic exposure and a lower likelihood of CYP-mediated drug interactions[100,101]. Despite these favorable

properties, all selected phytochemicals exhibited comparatively low VDss values, implying limited tumor tissue penetration and the need for formulation and structural optimization. Toxicological evaluation revealed that all selected ligands possessed a superior safety profile compared to the control compounds. None were predicted to be hepatotoxic, a major cause of late-stage drug development failure[102], and all demonstrated lower cardiotoxicity and mutagenic potential. The predicted biological activity further highlights their relevance in melanoma treatment. Although cytotoxicity data for A375 and A375-resistant (A375R) cell lines were unavailable, both of which are optimal models for the study's biological context[24], the server provided results for SK-MEL-1 cells harboring the $BRAF_{V600E}$ mutation[103]. All selected phytochemicals demonstrated moderate cytotoxic activity in this model, supporting their potential for further analyses.

Thermodynamic calculations provide insights into the reaction kinetics and molecular stability. More negative values from these calculations indicate a higher likelihood of binding to interacting molecules[104]. Based on this analysis, all the selected phytochemicals were predicted to be more reactive than the control compounds. Previous studies have demonstrated that compounds with higher dipole moments generally exhibit greater water solubility but reduced permeability through lipophilic membranes[105,106]. The lower dipole moments of the selected phytochemicals compared to the controls suggest an enhanced potential to access intracellular targets, such as EZH2. Furthermore, the selected phytochemicals displayed moderate HOMO-LUMO gaps, low hardness, high softness, and elevated electrophilicity compared to tazemetostat (CID: 66558664). These electronic properties indicate favorable polarizability and electron-accepting capacity, which align with the multiple hydrogen bonds and polar interactions observed in the docking poses, providing a plausible explanation for the high docking scores. However, these features may also indicate increased chemical reactivity or potential metabolic liabilities, necessitating experimental validation. The MEP analysis revealed that the oxygen atoms carried the most negative potential, whereas the hydrogen atoms were the most positive. Sotetsuflavone (CID: 5494868) exhibited the highest MEP values, whereas tazemetostat (CID: 66558664) exhibited the lowest. MEP mapping is a key tool for identifying electrophilic and nucleophilic regions and provides insights into the potential active sites for biological interactions[107].

Molecular dynamics (MD) simulation is a powerful approach in modern drug discovery that enables the evaluation of ligand-receptor binding energetics and kinetics, thereby assisting in the selection of optimal candidate molecules for further development[108]. Accordingly, all selected phytochemicals and control compounds were subjected to 100 ns MD simulations to assess the structural stability and interaction durability of the protein-ligand complexes under physiologically relevant conditions. The 100 ns simulation window was chosen based on prior studies that demonstrated its effectiveness in evaluating the inhibitory potential of phytochemicals[109,110]. Post-simulation analyses identified amentoflavone (CID: 5281600) as the most promising candidate, fulfilling the majority of the computational criteria for an effective EZH2 inhibitor. Lower Rg and SASA values indicate greater structural compactness[111,112], while a more negative MMPBSA binding energy reflects stronger ligand-protein affinity[66]. amentoflavone (CID: 5281600) consistently displayed the lowest average Rg, SASA, and MM/PBSA values among all the complexes, suggesting superior compactness and binding strength. Throughout the 100 ns simulation, the ligand maintained the highest and most persistent hydrogen bond count, further supporting stable ligand-protein interactions. PCA revealed a tightly clustered conformational landscape, indicative of stable complex dynamics. Although sotetsuflavone (CID: 5494868) showed the lowest RMSD and RMSF values, its frequent loss of hydrogen bonds suggested less stable polar anchoring, making it comparatively less reliable than amentoflavone (CID: 5281600). Podocarpusflavone A (CID: 5320644) exhibited results comparable to amentoflavone (CID: 5281600), with low RMSF and moderate Rg and SASA values, indicating substantial compactness and stability. It also maintained relatively consistent hydrogen bonding and formed a tight PCA cluster, ranking second only to amentoflavone (CID: 5281600) in terms of overall stability. In contrast, ginkgetin (CID: 5271805), despite exhibiting the best PCA clustering, demonstrated a higher RMSD (4.67 Å) and weaker MM/PBSA binding energy (− 16.07 kJ/mol), limiting its potential despite acceptable hydrogen bond persistence. Overall, the MD simulation results highlighted amentoflavone (CID: 5281600), a phytochemical derived from *Taxus baccata*, as the most promising lead for developing EZH2 inhibitors capable of overcoming melanoma therapy resistance.

5. Conclusions

Targeting EZH2 represents a promising therapeutic strategy for overcoming resistance to melanoma. However, the scarcity of approved EZH2 inhibitors and the limitations of SAM-competitive agents underscore the need for novel scaffolds. In this context, the present study screened 98 phytochemicals derived from *Taxus baccata* to identify potential candidates against EZH2, aiming to address therapeutic resistance in melanoma. Virtual screening and molecular docking analyses identified four phytochemicals–sotetsuflavone (CID: 5494868), ginkgetin (CID: 5271805), amentoflavone (CID: 5281600), and podocarpusflavone A (CID: 5320644)–with superior binding affinities and interaction profiles compared to standard inhibitors. ADME, toxicity, and biological activity predictions further supported their drug-likeness and safety, whereas quantum chemical and molecular dynamics analyses validated their stability and reactivity. Among these, amentoflavone (CID: 5281600) exhibited the most favorable overall properties, suggesting its potential as a lead EZH2 inhibitor. The *Taxus* genus, already known to yield clinically approved anticancer agents, adds credibility to the pharmacological potential of *T. baccata* phytochemicals. This study provides, for the first time, computational evidence highlighting the potential of *T. baccata* to target epigenetic regulators for cancer treatment.

However, computational methods have intrinsic limitations. While they offer efficient and cost-effective approaches for early drug discovery, their precision depends on data quality and algorithmic robustness. Experimental validation remains indispensable to confirm the predicted efficacy and pharmacokinetic behavior of these compounds[113,114]. In-vitro cytotoxic assays using A375 and A375-resistant (A375R) cell lines could verify their potential against resistant melanoma phenotypes, while melanoma xenograft models could assess tumor suppression and metastasis inhibition. Moreover, evidence suggests that EZH2 inhibitors may achieve maximal benefit when used in combination with other therapies[17]; thus, future studies should explore potential synergistic effects. Optimization of pharmacokinetic parameters, along with scalable extraction or synthesis processes, will be essential for translational development. Inter-individual variations influenced by genetic and environmental factors should also be considered to design personalized therapeutic strategies.

In conclusion, this study identified promising *Taxus baccata*-derived phytochemicals as potential EZH2 inhibitors, establishing a strong computational foundation for future experimental

validation. The integration of computer-aided drug design (CADD) has significantly accelerated lead identification and reduced the need for extensive synthesis and biological screening, with several marketed drugs discovered or optimized through such methods[115]. The present findings therefore hold promise for advancing novel therapeutic approaches against therapy-resistant melanoma.

Declaration

Acknowledgement

We sincerely extend our heartfelt gratitude and deep appreciation to CHIRAL Bangladesh and Centre for Bioinformatics Learning Advancement and Systematics Training (cBLAST), University of Dhaka for their high-performance computational assistance and collaboration in facilitating various aspects of the research. We are also grateful to Dr. Zeba Islam Seraj, Professor of Biochemistry and Molecular Biology, University of Dhaka for her encouragement and MD simulation software support. Their collective contributions played a pivotal role in the successful completion of this work.

Author Contribution

P.K. and M.S. conceptualized and designed the study; F.A.M., A.T.R., H.B.L., M.Z.A., M.A.M., U.M.P.K., F.M., S.S.C., S.A.S. performed data acquisition, analysis, and manuscript drafting; P.K. and M. S. performed critical revision and manuscript editing; M.J.H. was the supervisor and principal investigator. All authors participated in the study and approved the final submitted manuscript.

Data availability statement

All data used to support the results of this in silico study are included in this article.

Competing Interests

The authors declare no competing interests.

Funding

This research did not receive any specific grant from funding agencies in the public, commercial, or not-for-profit sectors.

References

1. Karami Fath, M. *et al.* Current understanding of epigenetics role in melanoma treatment and resistance. *Cancer Cell Int.* **22**, 313 (2022).
2. Kolathur, K. K. *et al.* Molecular Susceptibility and Treatment Challenges in Melanoma. *Cells* **13**, 1383 (2024).
3. Phillipps, J. *et al.* Efficacy of PARP inhibitor therapy after targeted BRAF/MEK failure in advanced melanoma. *Npj Precis. Oncol.* **8**, 187 (2024).
4. Melanoma of the Skin - Cancer Stat Facts. *SEER* https://seer.cancer.gov/statfacts/html/melan.html.
5. Skin Cancer Facts & Statistics. *The Skin Cancer Foundation* https://www.skincancer.org/skin-cancer-information/skin-cancer-facts/.
6. Subbiah, V., Baik, C. & Kirkwood, J. M. Clinical Development of BRAF plus MEK Inhibitor Combinations. *Trends Cancer* **6**, 797–810 (2020).
7. Fateeva, A., Eddy, K. & Chen, S. Current State of Melanoma Therapy and Next Steps: Battling Therapeutic Resistance. *Cancers* **16**, 1571 (2024).
8. Sanlorenzo, M. *et al.* Melanoma immunotherapy. *Cancer Biol. Ther.* **15**, 665–674 (2014).
9. Knight, A., Karapetyan, L. & Kirkwood, J. M. Immunotherapy in Melanoma: Recent Advances and Future Directions. *Cancers* **15**, 1106 (2023).
10. Li, W. *et al.* Evolving cancer resistance to anti-PD-1/PD-L1 antibodies in melanoma: Comprehensive insights with future prospects. *Crit. Rev. Oncol. Hematol.* **201**, 104426 (2024).
11. Huang, F., Santinon, F., Flores González, R. E. & Del Rincón, S. V. Melanoma Plasticity: Promoter of Metastasis and Resistance to Therapy. *Front. Oncol.* **11**, 756001 (2021).

12. Mahmoud, F. *et al.* Role of EZH2 histone methyltrasferase in melanoma progression and metastasis. *Cancer Biol. Ther.* **17**, 579–591 (2016).
13. Wagstaff, W. *et al.* Melanoma: Molecular genetics, metastasis, targeted therapies, immunotherapies, and therapeutic resistance. *Genes Dis.* **9**, 1608–1623 (2022).
14. FDA approves atezolizumab for BRAF V600 unresectable or metastatic melanoma | FDA. https://www.fda.gov/drugs/resources-information-approved-drugs/fda-approves-atezolizumab-braf-v600-unresectable-or-metastatic-melanoma.
15. Wang, X., Ma, S., Zhu, S., Zhu, L. & Guo, W. Advances in Immunotherapy and Targeted Therapy of Malignant Melanoma. *Biomedicines* **13**, 225 (2025).
16. Ferrucci, P. F., Lens, M. & Cocorocchio, E. Combined BRAF-Targeted Therapy with Immunotherapy in BRAF-Mutated Advanced Melanoma Patients. *Curr. Oncol. Rep.* **23**, 138 (2021).
17. Hanly, A. *et al.* Drugging the Epigenome: Overcoming Resistance to Targeted and Immunotherapies in Melanoma. *JID Innov.* **2**, 100090 (2022).
18. Rubanov, A., Berico, P. & Hernando, E. Epigenetic Mechanisms Underlying Melanoma Resistance to Immune and Targeted Therapies. *Cancers* **14**, 5858 (2022).
19. Tao, L. *et al.* Epigenetic regulation in cancer therapy: From mechanisms to clinical advances. *MedComm – Oncol.* **3**, e59 (2024).
20. Duan, R., Du, W. & Guo, W. EZH2: a novel target for cancer treatment. *J. Hematol. Oncol.J Hematol Oncol* **13**, 104 (2020).
21. Sabour-Takanlou, M., Sabour-Takanlou, L. & Biray-Avci, C. EZH2 -associated tumor malignancy: A prominent target for cancer treatment. *Clin. Genet.* **106**, 377–385 (2024).
22. Hoy, S. M. Tazemetostat: First Approval. *Drugs* **80**, 513–521 (2020).

23. Research, C. for D. E. and. FDA granted accelerated approval to tazemetostat for follicular lymphoma. *FDA* https://www.fda.gov/drugs/fda-granted-accelerated-approval-tazemetostat-follicular-lymphoma (2024).

24. Uebel, A. *et al.* Resistance to BRAF Inhibitors: EZH2 and Its Downstream Targets as Potential Therapeutic Options in Melanoma. *Int. J. Mol. Sci.* **24**, 1963 (2023).

25. Tiffen, J. C. *et al.* EZH2 as a mediator of treatment resistance in melanoma. *Pigment Cell Melanoma Res.* **29**, 500–507 (2016).

26. Chu, L. *et al.* EZH2 W113C is a gain-of-function mutation in B-cell lymphoma enabling both PRC2 methyltransferase activation and tazemetostat resistance. *J. Biol. Chem.* **299**, 103073 (2023).

27. Morschhauser, F. *et al.* Phase 2 Multicenter Study of Tazemetostat, an EZH2 Inhibitor, in Patients with Relapsed or Refractory Follicular Lymphoma. *Blood* **134**, 123–123 (2019).

28. Anju K Paul, Hridya Jayamohanan, & Keechilat Pavithran. Tazemetostat– A Drug review. *Int. J. Res. Pharm. Sci.* **12**, 894–898 (2021).

29. Konieczkowski, D. Systematic approaches to overcoming limitations of MAPK pathway inhibition in melanoma. http://nrs.harvard.edu/urn-3:HUL.InstRepos:11169802 (2013).

30. Othman, B. *et al.* Comprehensive pharmacokinetic profiling and molecular docking analysis of natural bioactive compounds targeting oncogenic biomarkers in breast cancer. *Sci. Rep.* **15**, 5426 (2025).

31. Mandour, Y. M., Refaat, E. & Hassanein, H. D. Anticancer activity, phytochemical investigation and molecular docking insights of Citrullus colocynthis (L.) fruits. *Sci. Rep.* **13**, 20038 (2023).

32. Sultan, R. *et al.* The anticancer potential of chemical constituents of Moringa oleifera targeting CDK-2 inhibition in estrogen receptor positive breast cancer using in-silico and in vitro approches. *BMC Complement. Med. Ther.* **23**, 396 (2023).

33. Jîjie, A.-R. *et al.* A Deep Dive into the Botanical and Medicinal Heritage of Taxus. *Plants* **14**, 1439 (2025).

34. Chandran, H., Meena, M., Barupal, T. & Sharma, K. Plant tissue culture as a perpetual source for production of industrially important bioactive compounds. *Biotechnol. Rep.* **26**, e00450 (2020).

35. Khanna, C., Rosenberg, M. & Vail, D. M. A Review of Paclitaxel and Novel Formulations Including Those Suitable for Use in Dogs. *J. Vet. Intern. Med.* **29**, 1006–1012 (2015).

36. Uddin, Md. M. *et al.* Molecular screening and dynamics simulation reveal potential phytocompounds in Swertia chirayita targeting the UspA1 protein of Moraxella catarrhalis for COPD therapy. *PLOS ONE* **20**, e0316275 (2025).

37. Straining, PharmD, R. & Eighmy, PharmD, W. Tazemetostat: EZH2 Inhibitor. *J. Adv. Pract. Oncol.* **13**, 158–163 (2022).

38. Kim, S. *et al.* PubChem Substance and Compound databases. *Nucleic Acids Res.* **44**, D1202–D1213 (2016).

39. O'Boyle, N. M. *et al.* Open Babel: An open chemical toolbox. *J. Cheminformatics* **3**, 33 (2011).

40. G09 | Gaussian.com. https://gaussian.com/glossary/g09/.

41. Branches, A. D. S. *et al.* DFT calculations, molecular docking, binding free energy analysis and cytotoxicity assay of 7,7-dimethylaporphine alkaloids with methylenedioxy ring in positions 1 and 2. *Comput. Theor. Chem.* **1233**, 114483 (2024).

42. Dallakyan, S. & Olson, A. J. Small-Molecule Library Screening by Docking with PyRx. in *Chemical Biology* (eds Hempel, J. E., Williams, C. H. & Hong, C. C.) vol. 1263 243–250 (Springer New York, New York, NY, 2015).

43. Guex, N., Peitsch, M. C. & Schwede, T. Automated comparative protein structure modeling with SWISS-MODEL and Swiss-PdbViewer: A historical perspective. *ELECTROPHORESIS* **30**, (2009).

44. Farooq, A. *et al.* Detection of probable phytochemical inhibitors targeting kallikrein related peptidase 7 (KLK7) in ovarian cancer through molecular dynamics and virtual screening approaches. *Sci. Rep.* **15**, 34749 (2025).

45. Wiederstein, M. & Sippl, M. J. ProSA-web: interactive web service for the recognition of errors in three-dimensional structures of proteins. *Nucleic Acids Res.* **35**, W407–W410 (2007).

46. Ye, B., Tian, W., Wang, B. & Liang, J. CASTpFold: Computed Atlas of Surface Topography of the universe of protein Folds. *Nucleic Acids Res.* **52**, W194–W199 (2024).

47. Nagasubramanian, K., Jha, S., Rathore, A. S. & Gupta, K. Identification of small molecule modulators of class II transactivator-I using computational approaches. *J. Biomol. Struct. Dyn.* **41**, 8349–8361 (2023).

48. Hussein, H. A. *et al.* PockDrug-Server: a new web server for predicting pocket druggability on holo and apo proteins. *Nucleic Acids Res.* **43**, W436–W442 (2015).

49. Eberhardt, J., Santos-Martins, D., Tillack, A. F. & Forli, S. AutoDock Vina 1.2.0: New Docking Methods, Expanded Force Field, and Python Bindings. *J. Chem. Inf. Model.* **61**, 3891–3898 (2021).

50. Pagadala, N. S., Syed, K. & Tuszynski, J. Software for molecular docking: a review. *Biophys. Rev.* **9**, 91–102 (2017).

51. Shahroz, M. M. *et al.* Novel and Potential Small Molecule Scaffolds as DYRK1A Inhibitors by Integrated Molecular Docking-Based Virtual Screening and Dynamics Simulation Study. *Molecules* **27**, 1159 (2022).

52. Daina, A., Michielin, O. & Zoete, V. SwissADME: a free web tool to evaluate pharmacokinetics, drug-likeness and medicinal chemistry friendliness of small molecules. *Sci. Rep.* **7**, 42717 (2017).

53. Al-Ahliyya Amman University & Azzam, K. A. SwissADME and pkCSM Webservers Predictors: an integrated Online Platform for Accurate and Comprehensive Predictions for In Silico ADME/T Properties of Artemisinin and its Derivatives. *Kompleks. Ispol'z. Miner. Syr'âComplex Use Miner. Resour. Shikisattardy Keshendi Paid.* **325**, 14–21 (2023).

54. Wang, C., Wang, X., Deng, Y., Hu, Y. & Hu, L. Network toxicology combined with molecular docking technology to explore the molecular mechanism of amatoxin causing liver injury. *Sci. Rep.* **15**, 26068 (2025).

55. Xiong, G. *et al.* ADMETlab 2.0: an integrated online platform for accurate and comprehensive predictions of ADMET properties. *Nucleic Acids Res.* **49**, W5–W14 (2021).

56. Banerjee, P., Kemmler, E., Dunkel, M. & Preissner, R. ProTox 3.0: a webserver for the prediction of toxicity of chemicals. *Nucleic Acids Res.* **52**, W513–W520 (2024).

57. Abdul-Hammed, M. *et al.* Virtual screening, ADMET profiling, PASS prediction, and bioactivity studies of potential inhibitory roles of alkaloids, phytosterols, and flavonoids against COVID-19 main protease (M^{pro}). *Nat. Prod. Res.* **36**, 3110–3116 (2022).

58. Baby, K. *et al.* Computational drug repurposing of Akt-1 allosteric inhibitors for non-small cell lung cancer. *Sci. Rep.* **13**, 7947 (2023).

59. Fahim, A. M., Dacrory, S. & Elsayed, G. H. Anti-proliferative activity, molecular genetics, docking analysis, and computational calculations of uracil cellulosic aldehyde derivatives. *Sci. Rep.* **13**, 14563 (2023).

60. Akash, S. *et al.* Novel computational and drug design strategies for inhibition of human papillomavirus-associated cervical cancer and DNA polymerase theta receptor by Apigenin derivatives. *Sci. Rep.* **13**, 16565 (2023).

61. Land, H. & Humble, M. S. YASARA: A Tool to Obtain Structural Guidance in Biocatalytic Investigations. in *Protein Engineering* (eds Bornscheuer, U. T. & Höhne, M.) vol. 1685 43–67 (Springer New York, New York, NY, 2018).

62. Prasasty, V. D. & Istyastono, E. P. Structure-Based Design and Molecular Dynamics Simulations of Pentapeptide AEYTR as a Potential Acetylcholinesterase Inhibitor. *Indones. J. Chem.* **20**, 953 (2020).

63. Verma, A. K. *et al.* Identification of 1, 2, 4-Triazine and Its Derivatives Against Lanosterol 14-Demethylase (CYP51) Property of Candida albicans: Influence on the Development of New Antifungal Therapeutic Strategies. *Front. Med. Technol.* **4**, 845322 (2022).

64. Wang, C. *et al.* Calculating protein–ligand binding affinities with MMPBSA: Method and error analysis. *J. Comput. Chem.* **37**, 2436–2446 (2016).

65. Shehzadi, K., Yu, M. & Liang, J. De Novo Potent Peptide Nucleic Acid Antisense Oligomer Inhibitors Targeting SARS-CoV-2 RNA-Dependent RNA Polymerase via Structure-Guided Drug Design. *Int. J. Mol. Sci.* **24**, 17473 (2023).

66. Ali, Md. A. *et al.* Exploring the Therapeutic Potential of Petiveria alliacea L. Phytochemicals: A Computational Study on Inhibiting SARS-CoV-2's Main Protease (Mpro). *Molecules* **29**, 2524 (2024).

67. Ahmed, Sk. F. *et al.* In silico identification of promising PD-L1 inhibitors from selected indian medicinal plants for treatment of triple negative breast cancer. *PLOS One* **20**, e0327475 (2025).

68. Valero-Mora, P. M. **ggplot2:** Elegant Graphics for Data Analysis. *J. Stat. Softw.* **35**, (2010).

69. Kwofie, S. K. *et al.* Pharmacoinformatics-based identification of potential bioactive compounds against Ebola virus protein VP24. *Comput. Biol. Med.* **113**, 103414 (2019).

70. Kwofie, S. K. *et al.* Cheminformatics-Based Identification of Potential Novel Anti-SARS-CoV-2 Natural Compounds of African Origin. *Molecules* **26**, 406 (2021).

71. Siddiquee, N. H. *et al.* Molecular activity of bioactive phytocompounds for inhibiting host cell attachment and membrane fusion interacting with West Nile Virus envelope glycoprotein. *PLOS One* **20**, e0321902 (2025).

72. Song, J. *et al.* Targeting epigenetic regulators as a promising avenue to overcome cancer therapy resistance. *Signal Transduct. Target. Ther.* **10**, 219 (2025).

73. Cazzato, G. *et al.* Epigenetics and Control of Tumor Angiogenesis in Melanoma: An Update with Therapeutic Implications. *Cancers* **16**, 2843 (2024).

74. Tigu, A. B. *et al.* Epigenetic Therapies in Melanoma—Targeting DNA Methylation and Histone Modification. *Biomedicines* **13**, 1188 (2025).

75. Roy, M. & Datta, A. Fundamentals of Phytochemicals. in *Cancer Genetics and Therapeutics* 49–81 (Springer Singapore, Singapore, 2019). doi:10.1007/978-981-13-9471-3_3.

76. Roy, M. & Datta, A. Drugs and Phytochemicals. in *Cancer Genetics and Therapeutics* 83–109 (Springer Singapore, Singapore, 2019). doi:10.1007/978-981-13-9471-3_4.

77. Roy, M. & Datta, A. Improvement of Cancer Therapy Using Phytochemicals. in *Cancer Genetics and Therapeutics* 139–164 (Springer Singapore, Singapore, 2019). doi:10.1007/978-981-13-9471-3_6.

78. Mora Lagares, L. *et al.* Homology Modeling of the Human P-glycoprotein (ABCB1) and Insights into Ligand Binding through Molecular Docking Studies. *Int. J. Mol. Sci.* **21**, 4058 (2020).

79. Wu, H. *et al.* Structure of the Catalytic Domain of EZH2 Reveals Conformational Plasticity in Cofactor and Substrate Binding Sites and Explains Oncogenic Mutations. *PLoS ONE* **8**, e83737 (2013).

80. Tan, J., Yan, Y., Wang, X., Jiang, Y. & Xu, H. E. EZH2: biology, disease, and structure-based drug discovery. *Acta Pharmacol. Sin.* **35**, 161–174 (2014).

81. Chammas, P., Mocavini, I. & Di Croce, L. Engaging chromatin: PRC2 structure meets function. *Br. J. Cancer* **122**, 315–328 (2020).

82. Tomassi, S., Romanelli, A., Zwergel, C., Valente, S. & Mai, A. Polycomb Repressive Complex 2 Modulation through the Development of EZH2–EED Interaction Inhibitors and EED Binders. *J. Med. Chem.* **64**, 11774–11797 (2021).

83. Tiffen, J., Gallagher, S. J. & Hersey, P. EZH 2: an emerging role in melanoma biology and strategies for targeted therapy. *Pigment Cell Melanoma Res.* **28**, 21–30 (2015).

84. Madushanka, A., Moura, R. T., Verma, N. & Kraka, E. Quantum Mechanical Assessment of Protein–Ligand Hydrogen Bond Strength Patterns: Insights from Semiempirical Tight-Binding and Local Vibrational Mode Theory. *Int. J. Mol. Sci.* **24**, 6311 (2023).

85. Ye, F., Huang, J., Wang, H., Luo, C. & Zhao, K. Targeting epigenetic machinery: Emerging novel allosteric inhibitors. *Pharmacol. Ther.* **204**, 107406 (2019).

86. Li, C. *et al.* Finding an easy way to harmonize: a review of advances in clinical research and combination strategies of EZH2 inhibitors. *Clin. Epigenetics* **13**, 62 (2021).

87. Feoli, A. *et al.* Lysine methyltransferase inhibitors: where we are now. *RSC Chem. Biol.* **3**, 359–406 (2022).

88. Han, Z. *et al.* Dual-Acting Peptides Target EZH2 and AR: A New Paradigm for Effective Treatment of Castration-Resistant Prostate Cancer. *Endocrinology* **164**, bqac180 (2022).

89. Groß, E. *et al.* SAM-Competitive EZH2-Inhibitors Induce Platinum Resistance by EZH2-Independent Induction of ABC-Transporters. *Cancers* **15**, 3043 (2023).

90. Zhang, T., Gong, Y., Meng, H., Li, C. & Xue, L. Symphony of epigenetic and metabolic regulation—interaction between the histone methyltransferase EZH2 and metabolism of tumor. *Clin. Epigenetics* **12**, 72 (2020).

91. Gilardini Montani, M. S., Benedetti, R. & Cirone, M. Targeting EZH2 in Cancer: Mechanisms, Pathways, and Therapeutic Potential. *Molecules* **29**, 5817 (2024).

92. Gan, L. *et al.* Epigenetic regulation of cancer progression by EZH2: from biological insights to therapeutic potential. *Biomark. Res.* **6**, 10 (2018).

93. Zhang, M.-Q. & Wilkinson, B. Drug discovery beyond the 'rule-of-five'. *Curr. Opin. Biotechnol.* **18**, 478–488 (2007).

94. Jia, C.-Y., Li, J.-Y., Hao, G.-F. & Yang, G.-F. A drug-likeness toolbox facilitates ADMET study in drug discovery. *Drug Discov. Today* **25**, 248–258 (2020).

95. Nguyen, T.-T.-L., Duong, V.-A. & Maeng, H.-J. Pharmaceutical Formulations with P-Glycoprotein Inhibitory Effect as Promising Approaches for Enhancing Oral Drug Absorption and Bioavailability. *Pharmaceutics* **13**, 1103 (2021).

96. Marchetti, S., Mazzanti, R., Beijnen, J. H. & Schellens, J. H. M. Concise Review: Clinical Relevance of Drug–Drug and Herb–Drug Interactions Mediated by the ABC Transporter ABCB1 (MDR1, P-glycoprotein). *The Oncologist* **12**, 927–941 (2007).

97. Karthika, C. *et al.* Multidrug Resistance of Cancer Cells and the Vital Role of P-Glycoprotein. *Life* **12**, 897 (2022).

98. Xiong, B., Lu, J.-J., Guo, H., Huang, M. & Li, T. Ginkgetin from Ginkgo biloba: mechanistic insights into anticancer efficacy. *Nat. Prod. Bioprospecting* **15**, 50 (2025).

99. Unger, M. Pharmacokinetic drug interactions involving *Ginkgo biloba*. *Drug Metab. Rev.* **45**, 353–385 (2013).

100. Yoshida, K. *et al.* Prediction of human pharmacokinetics for low-clearance compounds using pharmacokinetic data from chimeric mice with humanized livers. *Clin. Transl. Sci.* **15**, 79–91 (2022).

101. Orleni, M. & Beumer, J. H. Pharmacology and pharmacokinetics of tazemetostat. *Cancer Chemother. Pharmacol.* **93**, 509–517 (2024).

102. Gomez-Lechon, M. J., Lahoz, A., Gombau, L., Castell, J. V. & Donato, M. T. In Vitro Evaluation of Potential Hepatotoxicity Induced by Drugs. *Curr. Pharm. Des.* **16**, 1963–1977 (2010).

103. SK-MEL-1: Human Melanoma Cell Line (ATCC HTB-67) | Memorial Sloan Kettering Cancer Center. https://www.mskcc.org/research-advantage/support/technology/tangible-material/human-melanoma-cell-line-sk-mel-1.

104. Rahman, M. S. *et al.* Epitope-based chimeric peptide vaccine design against S, M and E proteins of SARS-CoV-2 etiologic agent of global pandemic COVID-19: an in silico approach. *PeerJ* **8**, e9572 (2020).

105. Das, A., Das, A. & Banik, B. K. Influence of dipole moments on the medicinal activities of diverse organic compounds. *J. Indian Chem. Soc.* **98**, 100005 (2021).

106. Pereira, F. & Aires-de-Sousa, J. Machine learning for the prediction of molecular dipole moments obtained by density functional theory. *J. Cheminformatics* **10**, 43 (2018).

107. Sheeja Mol, G. P. *et al.* Structural activity, fungicidal activity and molecular dynamics simulation of certain triphenyl methyl imidazole derivatives by experimental and computational spectroscopic techniques. *Spectrochim. Acta. A. Mol. Biomol. Spectrosc.* **212**, 105–120 (2019).

108. Salo-Ahen, O. M. H. *et al.* Molecular Dynamics Simulations in Drug Discovery and Pharmaceutical Development. *Processes* **9**, 71 (2020).

109. Alanzi, A., Moussa, A. Y., Mothana, R. A., Abbas, M. & Ali, I. In silico exploration of PD-L1 binding compounds: Structure-based virtual screening, molecular docking, and MD simulation. *PLOS ONE* **19**, e0306804 (2024).

110. Binshaya, A. S., Alkahtani, O. S., Aldakheel, F. M., Hjazi, A. & Almasoudi, H. H. Structure-based multitargeted docking screening, pharmacokinetics, DFT, and dynamics simulation studies reveal mitoglitazone as a potent inhibitor of cellular survival and stress response proteins of lung cancer. *Med. Oncol.* **41**, 101 (2024).

111. Islam, Md. A. *et al.* In-silico study unveils potential phytocompounds in Andrographis paniculata against E6 protein of the high-risk HPV-16 subtype for cervical cancer therapy. *Sci. Rep.* **14**, 17182 (2024).

112. Sahu, S. N., Mishra, B., Sahu, R. & Pattanayak, S. K. Molecular dynamics simulation perception study of the binding affinity performance for main protease of SARS-CoV-2. *J. Biomol. Struct. Dyn.* **40**, 2444–2459 (2022).

113. Sur, S. & Nimesh, H. Challenges and limitations of computer-aided drug design. in *Advances in Pharmacology* vol. 103 415–428 (Elsevier, 2025).

114. Shah, A. & Jain, M. Limitations and future challenges of computer-aided drug design methods. in *Computer Aided Drug Design (CADD): From Ligand-Based Methods to Structure-Based Approaches* 283–297 (Elsevier, 2022). doi:10.1016/B978-0-323-90608-1.00006-X.

115. Computer-Aided Drug Design - an overview | ScienceDirect Topics. https://www.sciencedirect.com/topics/pharmacology-toxicology-and-pharmaceutical-science/computer-aided-drug-design.

Tables

Table 1.

Physicochemical property evaluation of the shortlisted phytochemicals and reference inhibitors

No	Compounds	MW (g/mol)	Heavy atoms	Aromatic Heavy	Rotatabl	H-bond	H-bond	TPSA (Å²)	Lipophili city	Water Solubilit	Class of Water Solubilit
1.	Sotetsuflavone (CID: 5494868)	552.48	41	32	4	10	5	170.80	4.04	-6.96	Poorly soluble
2.	Ginkgetin (CID: 5271805)	566.51	42	32	5	10	4	159.80	4.34	-7.17	Insoluble
3.	Amentoflavone (CID: 5281600)	538.46	40	32	3	10	6	181.80	3.62	-6.75	Poorly soluble
4.	Podocarpusflavone A (CID: 5320644)	552.48	41	32	4	10	5	170.80	4.03	-6.96	Poorly soluble
5.	Tazemetostat (CID: 66558664)	572.74	42	18	10	5	2	86.90	4.39	-5.68	Poorly soluble
6.	GSK 126 (CID: 68210102)	526.67	39	21	8	4	3	95.05	4.04	-5.41	Poorly soluble

Table 2.

Drug-likeness and medicinal chemistry profile of the shortlisted phytochemicals and reference inhibitors.

No	Name	Lipinski	Bioavailability Score	PAINS	Synthetic accessibility
1.	Sotetsuflavone (CID: 5494868)	Yes; 1 violation	0.55	0	4.37
2.	Ginkgetin (CID: 5271805)	Yes; 1 violation	0.55	0	4.50

3.	Amentoflavone (CID: 5281600)	No; 2 violations	0.55	0	4.27
4.	Podocarpusflavone A (CID: 5320644)	Yes; 1 violation	0.55	0	4.31
5.	Tazemetostat (CID: 66558664)	Yes; 1 violation	0.55	0	4.43
6.	GSK 126 (CID: 68210102)	Yes; 1 violation	0.55	0	4.65

Table 3.

Evaluation of ADME properties of the selected phytochemicals and the controls.

		Absorption				Distribution		Metabolism							Excretion	
No	CID	Intestina l [illegible]	Pglycop rotein [illegible]	Pglycop rotein I [illegible]	Pglycoprote in II inhibitor	VDss	BBB Permeabil ity	CYP 2D6 subst	CYP 3A4 subst	CYP 1A2 inhib	CYP 2C19 inhib	CYP 2C9 inhi	CYP 2D6 inhib	C YP 3A 4 inh	Total Cleara nce	Renal OCT2 substrat e
1	Sotetsufla vone (CID:	82.32 5	Yes	No	Yes	- 2.7 35	-1.19	No	Ye s	No	No	N o	No	N o	0.6 17	No
2	Ginkgetin (CID: 5271805)	95.37 6	No	Yes	Yes	- 1.2 74	-1.884	No	Ye s	No	No	Y es	No	N o	0.6 46	No
3	Amentofl avone (CID:	84.35 6	Yes	Yes	Yes	- 1.0 66	-1.653	No	Ye s	No	No	N o	No	N o	0.4 84	No
4	Podocarp usflavone A (CID:	79.68 2	Yes	Yes	Yes	- 1.2 57	-1.732	No	Ye s	No	No	Y es	No	N o	0.6 15	No
5	Tazemeto stat (CID	91.38 1	Yes	Yes	Yes	1.2 57	-0.815	No	Ye s	No	Ye s	Y es	No	Y e s	0.8 67	No
6	GSK 126 (CID: 68210102	91.54 4	Yes	Yes	Yes	1.2 31	-0.934	No	Ye s	No	No	Y es	No	Y e s	0.8 1	No

Table 4.

Predicted antineoplastic activity of the selected phytochemicals and the controls against melanoma.

Compounds		Antineoplastic (Melanoma)	
No	Name	Pa	Pi
1.	Sotetsuflavone (CID: 5494868)	0.367	0.014
2.	Ginkgetin (CID: 5271805)	0.353	0.015
3.	Amentoflavone (CID: 5281600)	0.353	0.015
4.	Podocarpusflavone A (CID: 5320644)	0.358	0.014
5.	Tazemetostat (CID: 66558664)	N/A	N/A
6.	GSK 126 (CID: 68210102)	N/A	N/A

Table 5.

Predicted toxicological profiles of the shortlisted compounds and controls

No	Name	Rat Oral Acute Toxicity	hERG Inhibition	Human hepatotoxicity (H-HT)	Carcinogenicity	Cytotoxicity	Mutagenicity

1.	Sotetsuflavone (CID: 5494868)	Low (0.06)	Low (0.07)	Low (0.12)	Low (0.04)	Inactive (0.93)	Inactive (0.81)
2.	Ginkgetin (CID: 5271805)	Low (0.06)	Low (0.04)	Low (0.17)	Low (0.04)	Inactive (0.93)	Inactive (0.80)
3.	Amentoflavone (CID: 5281600)	Low (0.06)	Low (0.09)	Low (0.14)	Low (0.04)	Inactive (0.98)	Inactive (0.71)
4.	Podocarpusflavone A (CID: 5320644)	Low (0.06)	Low (0.06)	Low (0.17)	Low (0.03)	Inactive (0.93)	Inactive (0.81)
5.	Tazemetostat (CID: 66558664)	High (0.92)	Moderate (0.63)	High (0.86)	Low (0.07)	Inactive (0.65)	Inactive (0.67)
6.	GSK 126 (CID: 68210102)	Moderate (0.30)	High (0.70)	High (0.98)	Low (0.06)	Inactive (0.64)	Active (0.57)

Table 6.

Predicted cytotoxicity of shortlisted compounds and controls against skin tumor and non-tumor cell lines using CLC-Pred (Pa > Pi).

		Tumor Cell-lines			Normal Cell-lines		
No	Name	Pa	Pi	Cell line	Pa	Pi	Cell line
1.	Sotetsuflavone (CID: 5494868)	0.254	0.135	M19-MEL	0.190	0.015	HaCaT
		0.208	0.146	G-361	0.122	0.066	CRL-7065
		0.205	0.16	SK-MEL-28	0.065	0.059	HS27
		0.186	0.166	SK-MEL-2	-	-	-
		0.371	0.108	SK-MEL-1	-	-	-
2.	Ginkgetin (CID: 5271805)	0.236	0.154	M19-MEL	0.185	0.016	HaCaT
		0.210	0.153	SK-MEL-28	0.122	0.066	CRL-7065
		0.197	0.167	G-361	-	-	-
		0.190	0.161	SK-MEL-2	-	-	-
		0.363	0.119	SK-MEL-1	-	-	-
3.	Amentoflavone (CID: 5281600)	0.236	0.098	G-361	0.204	0.012	HaCaT
		0.078	0.037	SK-MEL-103	0.119	0.076	CRL-7065
		0.384	0.091	SK-MEL-1	-	-	-
4.	Podocarpusflavone A (CID: 5320644)	0.218	0.179	M19-MEL	0.185	0.016	HaCaT
		0.205	0.142	SK-MEL-2	0.118	0.077	CRL-7065
		0.201	0.159	G-361	0.068	0.054	HS27
		0.198	0.169	SK-MEL-28	-	-	-
		0.192	0.183	Malme-3M	-	-	-
		0.366	0.114	SK-MEL-1	-	-	-

5.	Tazemetostat (CID: 66558664)	N/A	N/A	N/A	N/A	N/A	N/A
6.	GSK 126 (CID: 682101020)	N/A	N/A	N/A	N/A	N/A	N/A

Table 7.

Calculated frontier molecular orbital (FMO) energies and associated global reactivity descriptors.

Name	E_{HOMO}	E_{LUMO}	I	A	E_{gap}	μ	X	H	ω	Σ
Sotetsuflavone (CID: 5494868)	−0.227	−0.083	0.227	0.083	0.144	−0.155	0.155	0.072	0.166	13.888
Ginkgetin (CID: 5271805)	−0.226	−0.083	0.226	0.083	0.143	−0.154	0.154	0.071	0.166	13.986
Amentoflavone (CID: 5281600)	−0.229	−0.084	0.229	0.084	0.145	−0.156	0.156	0.072	0.168	13.7931
Podocarpusflavone A (CID: 5320644)	−0.229	−0.085	0.229	0.085	0.144	−0.157	0.157	0.072	0.171	13.888
Tazemetostat (CID: 66558664)	−0.198	−0.040	0.198	0.040	0.158	−0.119	0.119	0.079	0.089	12.658
GSK 126 (CID: 682101020)	−0.182	−0.042	0.182	0.042	0.140	−0.112	0.112	0.070	0.0896	14.285

Table 8.

The average values with standard deviations (SD) of RMSD, RMSF, Rg, SASA, H-bonds, and MM-PBSA-based binding free energy (ΔG) for all protein–ligand complexes

Complex	RMSD	RMSF	Rg	SASA	H bond	MMPBSA
Sotetsuflavone (CID:5494868)	2.835 ± 0.415	1.719 ± 0.750	18.956 ± 0.240	11929.186 ± 184.157	422.736 ± 12.025	− 67.531 ± 59.585

Ginkgetin (CID:5271805)	4.668 ± 1.320	2.881 ± 1.672	19.359 ± 0.302	12102.725 ± 229.820	430.569 ± 11.811	− 16.066 ± 46.801
Amentoflavone (CID:5281600)	3.267 ± 0.407	2.154 ± 1.042	18.879 ± 0.274	11786.486 ± 293.281	424.599 ± 12.094	− 101.725 ± 42.594
Podocarpusflavone A (CID:5320644)	3.553 ± 0.554	1.955 ± 1.123	18.868 ± 0.160	11896.720 ± 241.234	424.526 ± 12.839	− 45.320 ± 36.292
Tazemetostat (CID:66558664)	3.804 ± 0.751	2.316 ± 1.314	19.359 ± 0.297	12352.470 ± 263.408	422.920 ± 11.292	+7.377 ± 40.474
GSK 126 (CID:68210102)	3.208 ± 0.673	2.063 ± 1.152	19.133 ± 0.247	12134.507 ± 199.646	429.242 ± 14.325	− 67.768 ± 40.508

Figure Legends

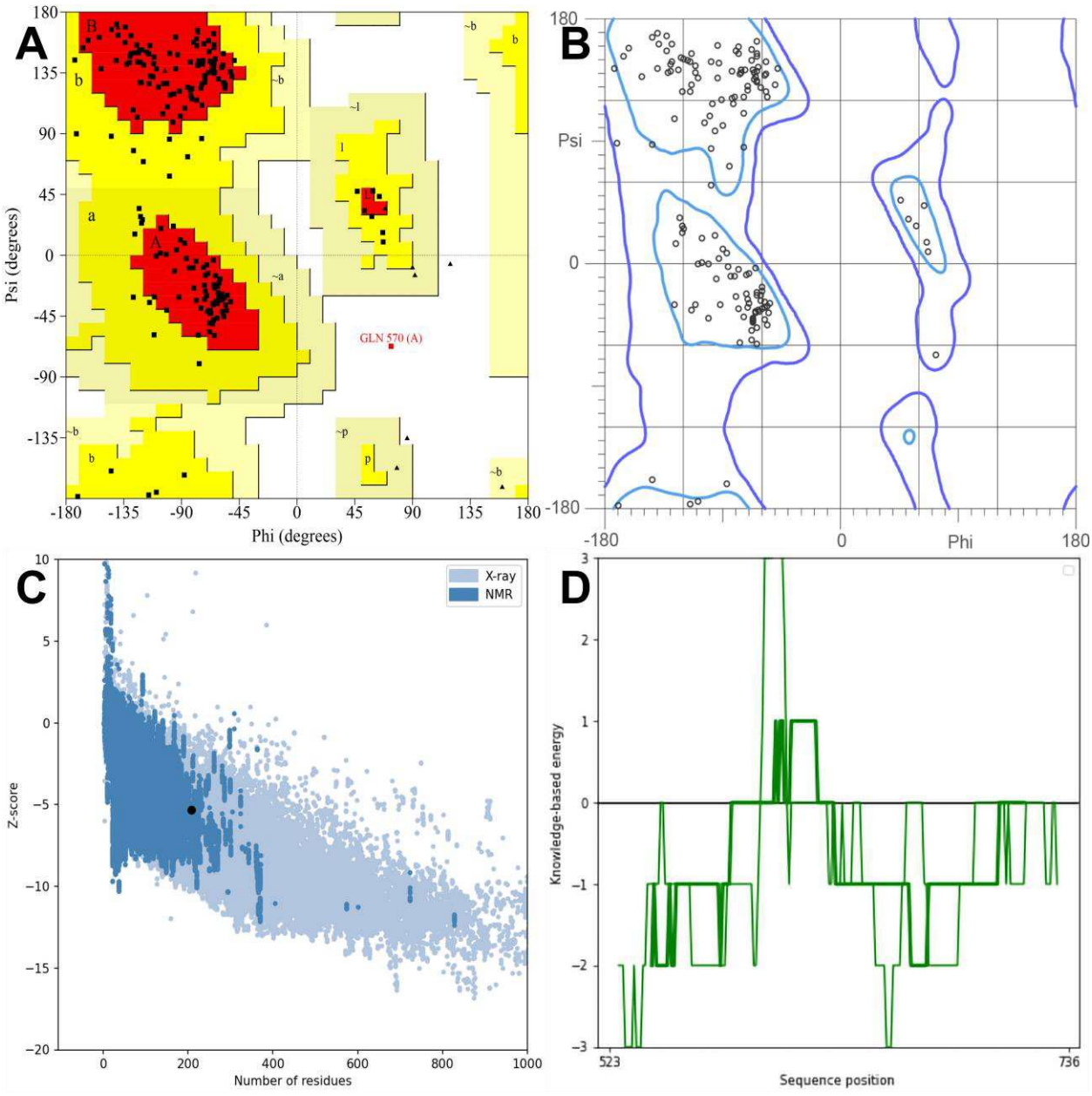

Figure 1: Protein validation plots. (A) PROCHECK Ramachandran plot, (B) MolProbity Ramachandran plot, (C) ProSA-Web Z-score, and (D) ProSA-Web local quality profile

.

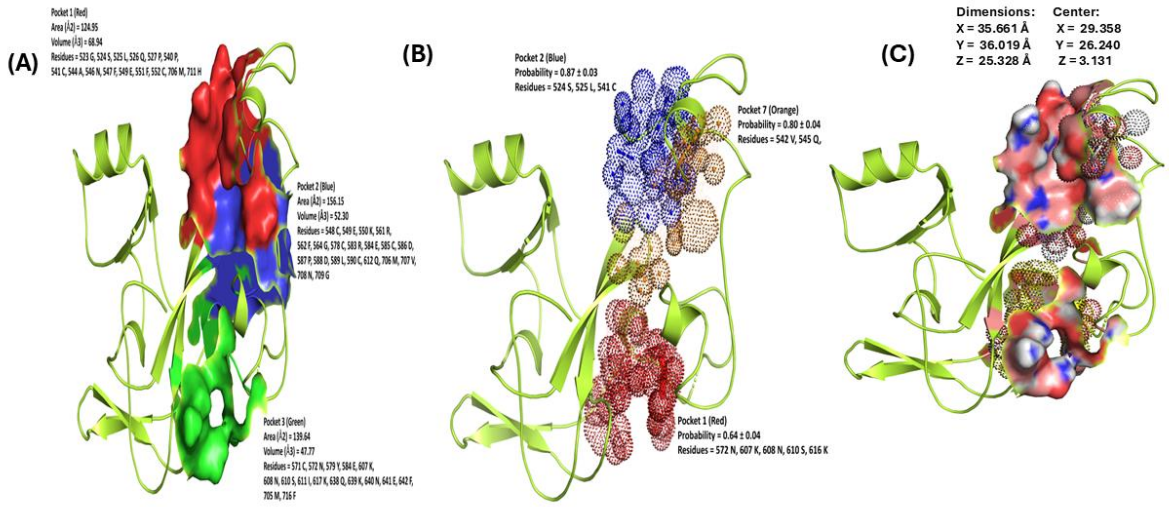

Figure 2: Active site prediction and grid generation. (A) Top 3 pockets predicted by CASTpFold, (B) Top 3 druggable pockets predicted by PockDrug, and (C) Grid box parameters with surface representation of the target region.

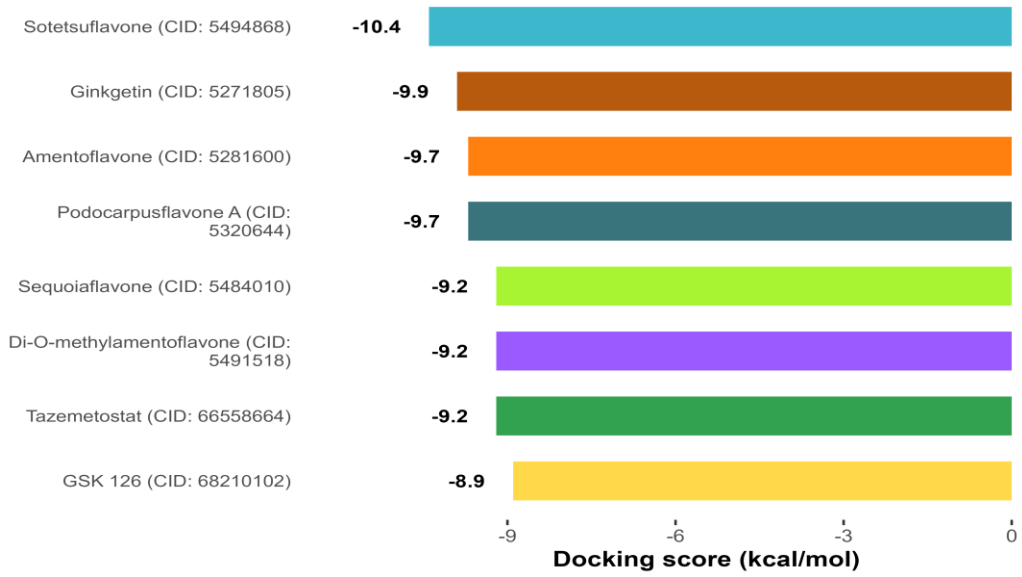

Figure 3: Docking scores (kcal/mol) of top *T. baccata* compounds compared with control ligands. Negative values above each bar denote the binding affinities. Tazemetostat and GSK126 served as controls.

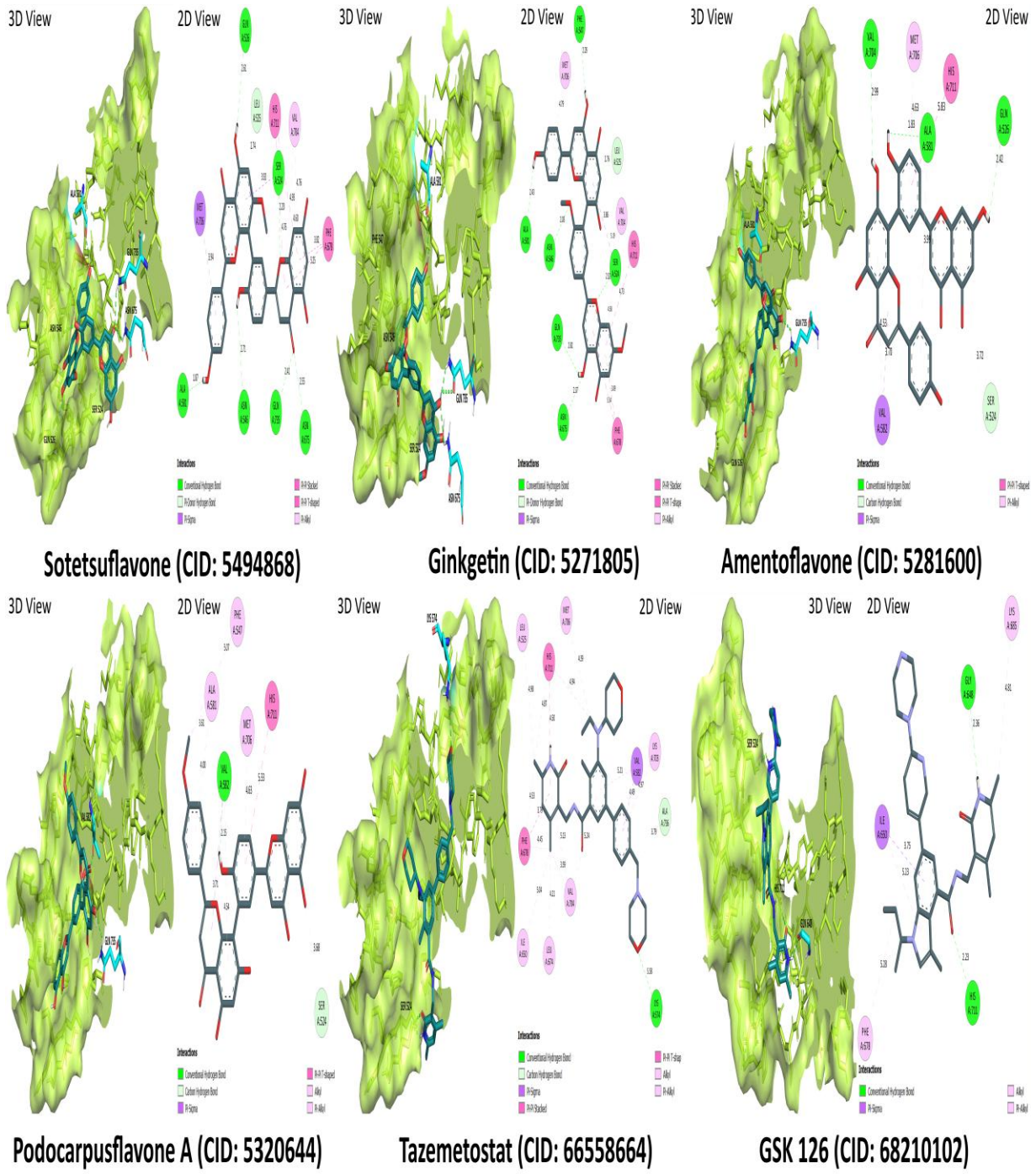

Figure 4: Structural representation of shortlisted ligands and control compounds bound to the target protein active site. The left panel of each image depicts the 3D surface view of the ligand within the protein's active site, while the right panel illustrates the corresponding 2D protein-ligand interaction map.

.

.

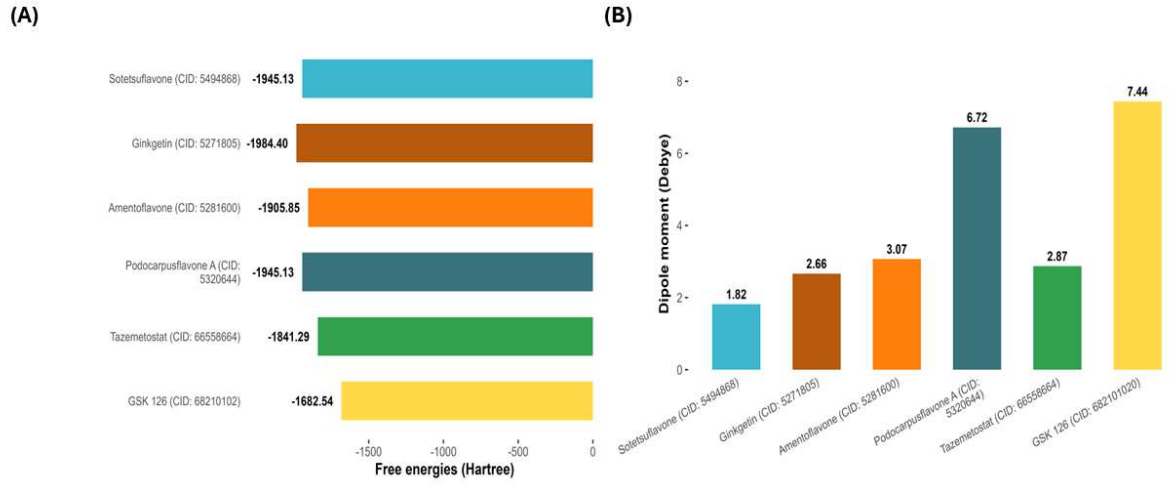

Figure 5: Thermodynamic properties of the shortlisted compounds from *T. baccata* and the controls. (A) Gibbs free energy values. (B) Dipole moment values

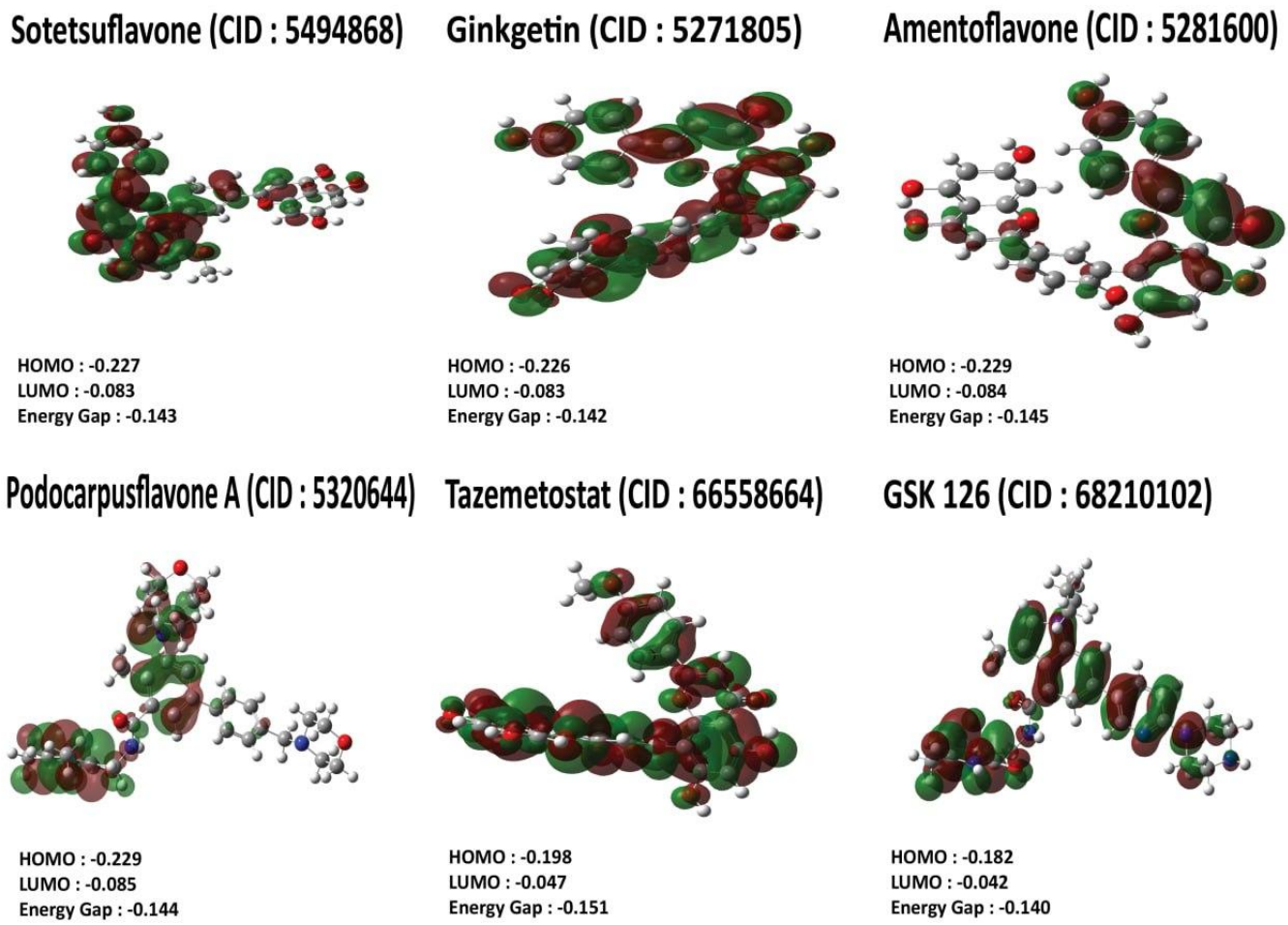

Figure 6: Frontier molecular orbitals (HOMO-LUMO) and energy gaps of the shortlisted phytochemicals and controls. Depicted are the HOMO and LUMO distributions with respective energy gap (ΔE) values, representing the electronic properties and stability of each compound.

.

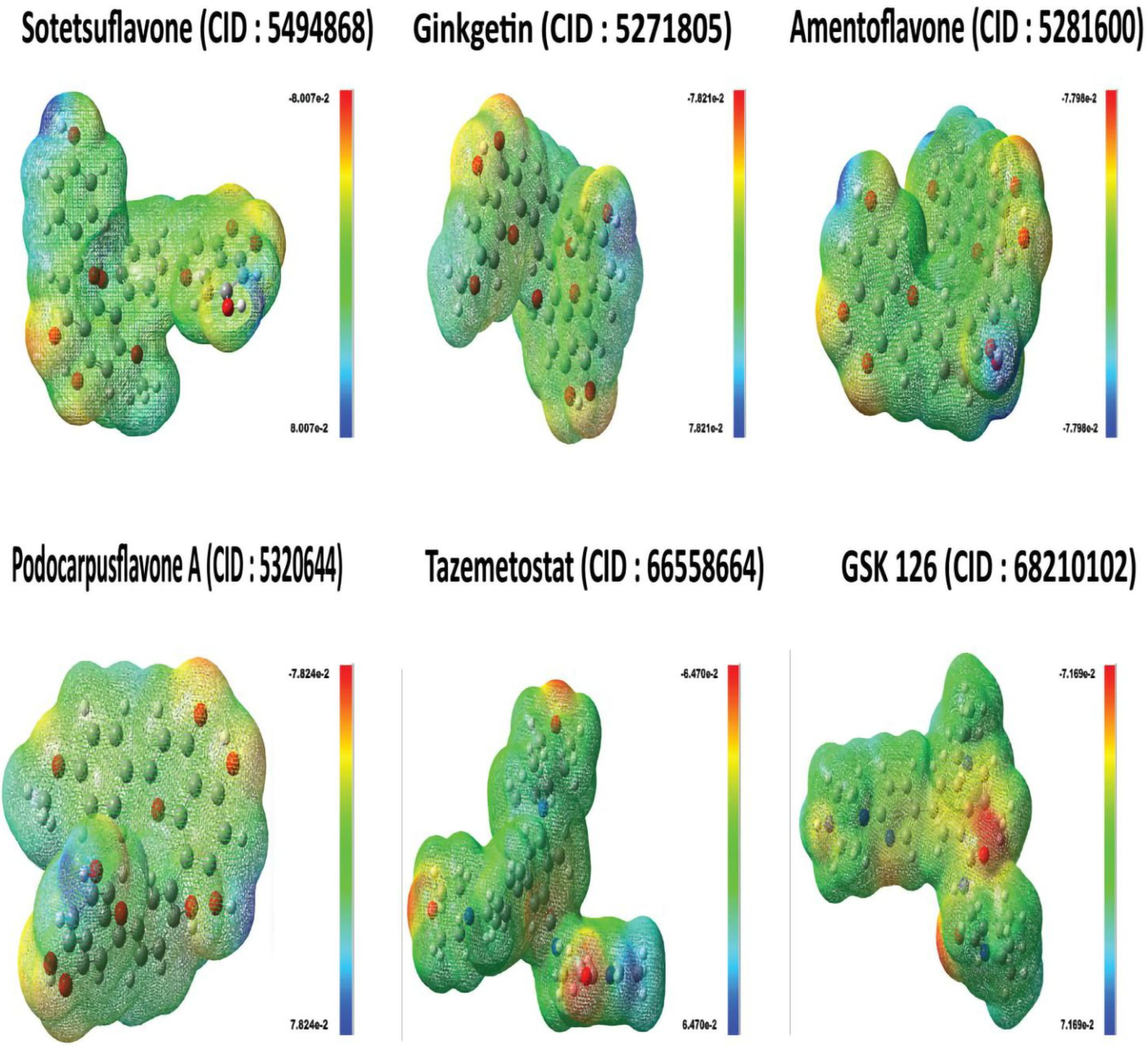

Figure 7: Molecular electrostatic potential (MEP) maps of shortlisted compounds from *T. baccata*. The MEP maps illustrate the charge distribution across each molecule: blue indicates regions of positive potential (low electron density), red denotes negative potential (high electron density

.

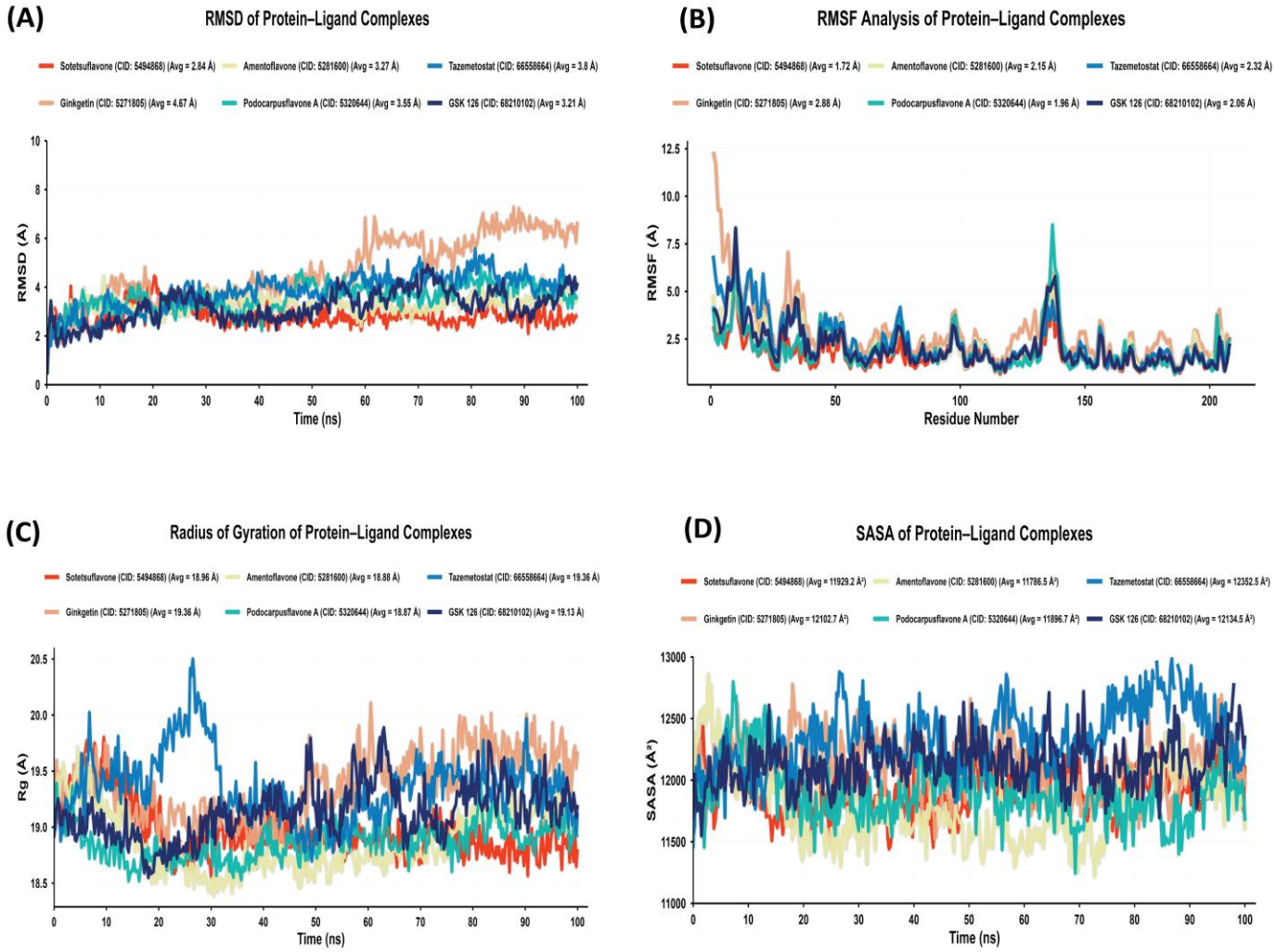

Figure 8: Molecular Dynamic Simulation Analysis Structural Stability (100 ns) (A) Root mean square deviation (RMSD) (B) Root mean square fluctuation (RMSF) (C) Radius of gyration (Rg) analysis (D) Solvent accessible surface area (SASA)

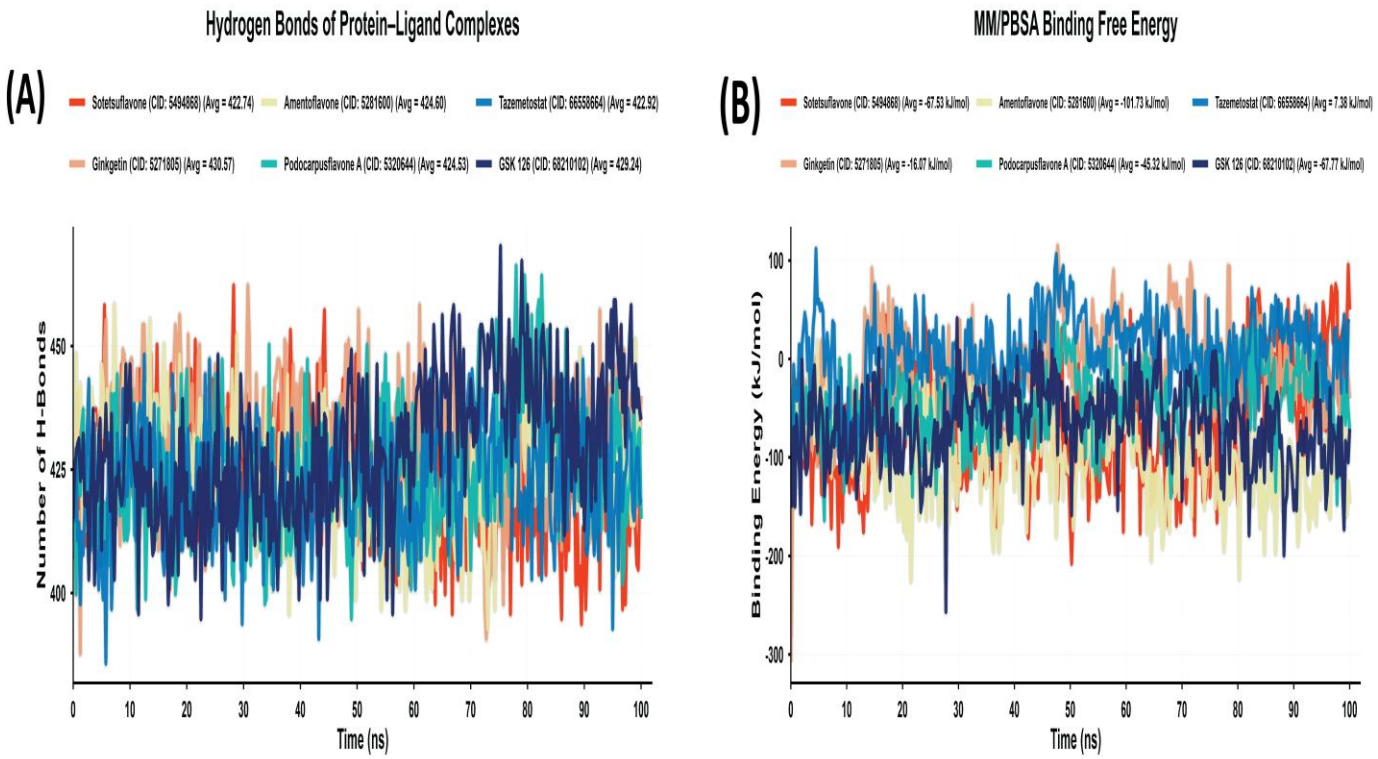

Figure 9: Molecular Dynamic Simulation Interaction Stabilities (100 ns). (A) Hydrogen bond analysis (B) Binding free energy MMPBSA

.

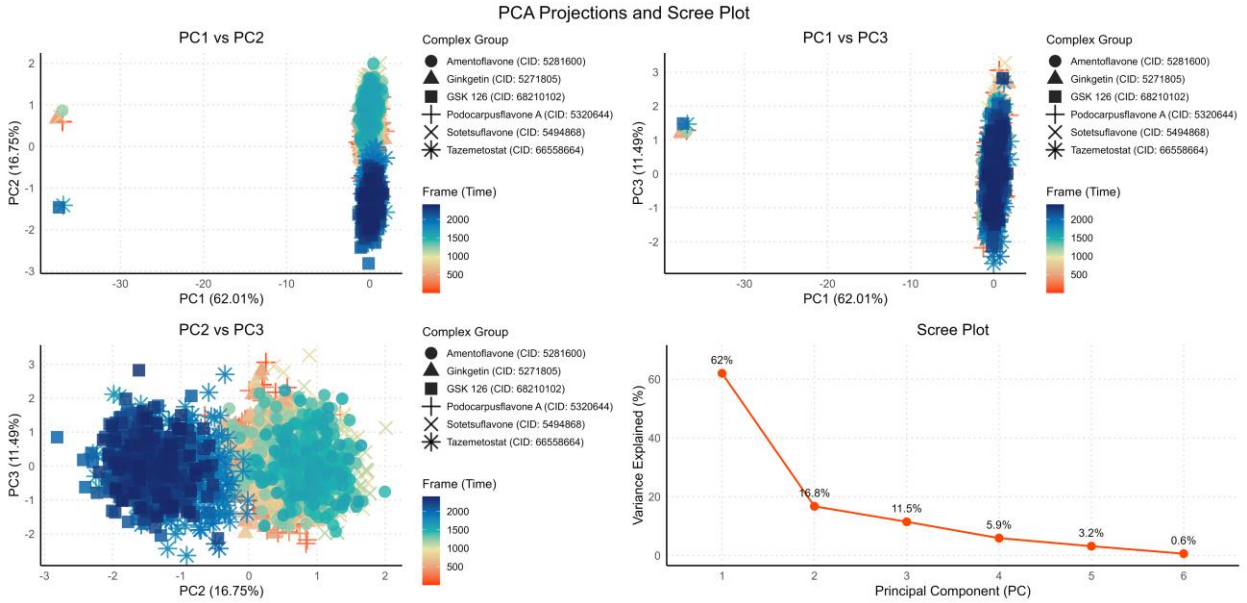

Figure 10: Principal Component Analysis (PCA) of six complexes from 100 ns molecular dynamics simulations The PCA plots depict the structural dynamics and conformational variability of the six protein–ligand complexes over the 100 ns simulation, highlighting dominant motions and collective fluctuations in each system.

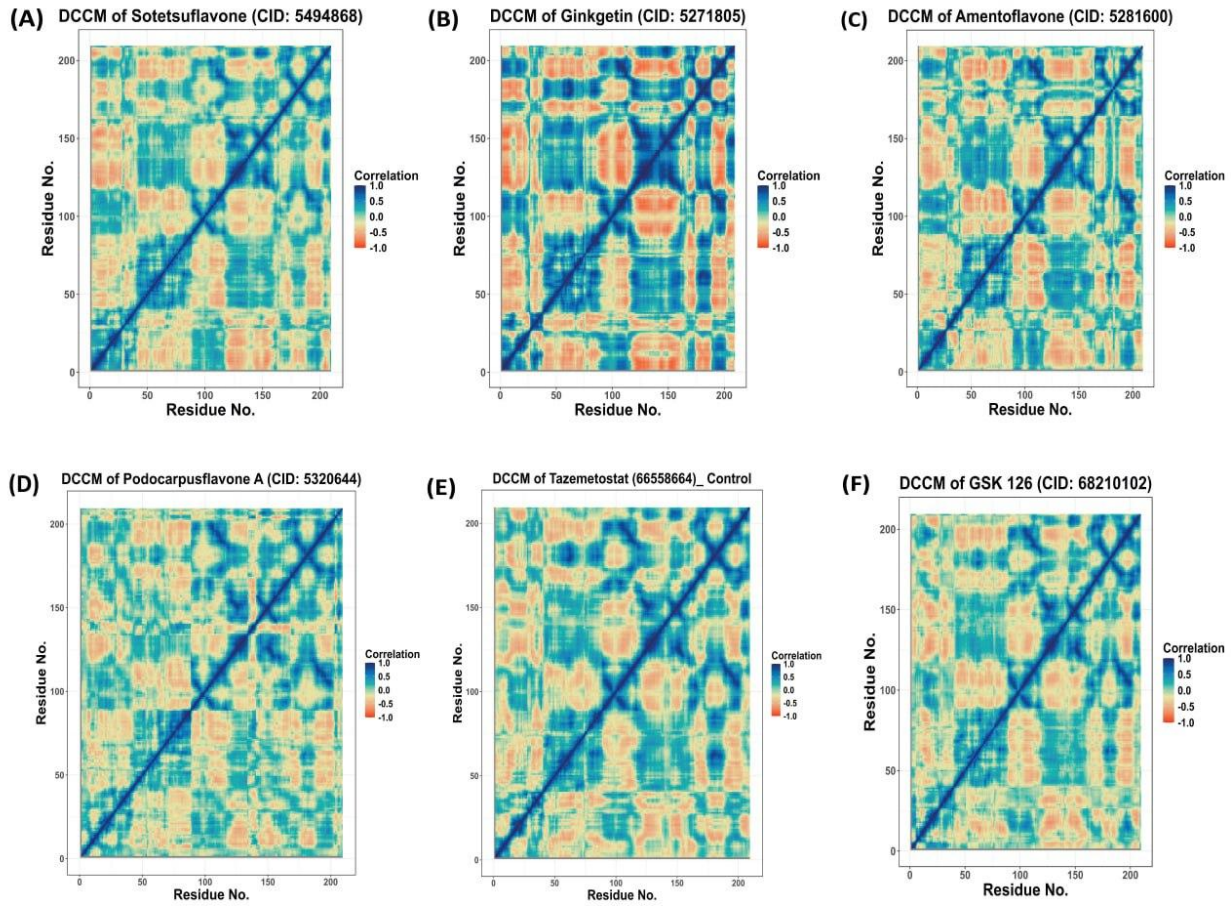

Figure 11: Dynamic Cross-Correlation Matrix (DCCM) analysis of protein-ligand complexes from 100 ns molecular dynamics simulations. The DCCM plots illustrate correlated and anti-correlated atomic motions within the protein structures over 100 ns, revealing regions of concerted dynamics and functional connectivity in each complex.

Supplementary Files

This is a list of supplementary files associated with this preprint. Click to download.

- SuplimentaryFile.docx